THE LAGRANGIAN PROPERTIES OF THE FLOW WEST OF OAHU

A THESIS SUBMITTED TO THE GRADUATE DIVISION OF THE
UNIVERSITY OF HAWAIʻI IN PARTIAL FULFILLMENT
OF THE REQUIREMENTS FOR THE DEGREE OF

MASTER OF SCIENCE

IN

OCEANOGRAPHY

DECEMBER 2009

By

Victoria C. Futch

Thesis Committee:

Pierre Flament, Chairperson
Mark Merrifield
Niklas Schneider

We certify that we have read this thesis and that, in our opinion, it is satisfactory in scope and quality as a thesis for the degree of Master of Science in Oceanography.

THESIS COMMITTEE

Chairperson

Contents

Acknowledgements

First I'd like to that the U.S. Coast Guard for funding my graduate degree and providing me with the time and resources to advance my education.

I also must acknowledge my advisor, Dr. Pierre Flament, for the constant support and encouragement during my short stay as a Master's student, and for inspiring me to continue my education past a master's level. Thanks to Cedric Chavanne for mentoring me along the way and allowing me to build on your past work. To the lab, thanks for all the help and the laughs.

Lastly, thanks to my family and husband for the moral support necessary to accomplish such a hefty goal.

Abstract

The presence of an island in the path of a major current or steady wind regime creates complex dynamics in the lee of the island where the flow has been disrupted by topography. In this study, two High Frequency Radars were established on the leeward side of the island of Oahu, in the subtropical Pacific gyre, from September 2002 until May 2003. Due to the high resolution of the High Frequency Radar velocity data, smaller dispersion patterns can be examined. Here, the Lagrangian Rate of Separation and velocity gradient tensor properties were used to identify coherent structures in the flow that affected dispersion in the velocity field in the lee of Oahu. A new method, called an Instantaneous Rate of Separation, was derived from the relationship between the Lagrangian Rate of Separation and the components of the velocity gradient tensor. The Instantaneous Rate of Separation correlated well with the Lagrangian Rate of Separation under most circumstances. Coherent structures were visible in the flow for most of the time period analyzed, with significant features noted during eddy events and localized fronts. During steady flow without unique velocity features, coherent structures were not easily visible in the flow patterns.

List of Figures

Chapter 1

Introduction

Understanding how particles or objects disperse under different conditions has many practical applications, including search and rescue operations, marine pollution response, and larval drift and predation. The fate of two particles in a velocity field can be extremely different even if the particles started relatively near each other (Lekien, et al., 2005). Due to this strong dependence on initial conditions, analyzing dispersion patterns can be difficult using only drift trajectories. Instead, it has become more common to use patterns in the flow to determine transport barriers, or coherent structures which will affect particles in a wider ranging area. In previous studies, such as Coulliette et al., 2007 and Lekein et al., 2005, dispersion of a pollutant was correlated with the appearance of Lagrangian coherent structures in the flow that acted as transport barriers for particles. d'Ovidio et al., 2004 and d'Ovidio et al., 2007 used persistent unstable and stable manifolds, calculated using a Finite Size Lyapunov Exponent, in the flow to determine transport barriers for particles in the Mediterranean Sea.

In this paper, velocity data gathered from High Frequency Radars is used to look at dispersion patterns in the lee of an island. Established methods of identifying regions of divergence or convergence in a flow field are used to identify patterns unique to island dynamics that affect the dispersion of particles. Chapter 2 provides a theoretical background in dispersion theory. Chapter 3 describes the methods used to identify regions of divergence or convergence, The Lagrangian Rate of Separation and velocity gradient tensor components. A new variable called the Instantaneous Rate of Separation is defined from the relationship between the Lagrangian Rate of Separation and velocity gradient tensor. Chapter 4 details the general properties of the flow in the HF Radar coverage area , as well as identifies coherent structures and patterns in the flow. Coherent structures formed during an eddy event and the appearance of a localized front are discussed in Chapter 5. Chapter 6 details the importance of tides on dispersion in this region. Finally, Chapter 7 concludes the results and discusses suggestions for future work.

Chapter 2

Background

2.1 Basis for a study of dispersion

Understanding how objects on the ocean surface will drift subject to different physical conditions has many applications. From larval transport studies to oil spill recovery to search and rescue operations, understanding Lagrangian movement on the ocean's surface is vital to success. An interesting search and rescue case involving applications of drift prediction occurred off the northern most point of the Island of Hawaii. A kayaker went missing off Upolu Point and the Coast Guard was called to find the missing person. The Coast Guard deployed two Self Locating Datum Marker Buoys (SLDMBs) 6.8 nautical miles apart off Upolu Point (Fig. 1). One SLDMB turned to the east and drifted north-east towards the eastern side of Maui while the second SLDMB made a turn to the south-west and into the lee of the islands. The 180° difference in trajectories significantly increased the Coast Guard's search area. Without amplifying information or higher quality current data, little could be done to reduce the uncertainty of the lost kayaker's path through the water. The kayaker was never found. Here, methods used to predict and understand particle separation rates are studied to enhance our ability to accurately predict dispersion.

2.2 Particle dispersion theory

In order to simplify the problem, objects on the ocean's surface are reduced to infinitesimally small particles. By reducing the problem to particle motion, the effect of wind on objects in the water is removed, focusing the problem on the effect of surface currents alone. For this simplified scenario, the Lagrangian equation of motion for each infinitesimally small particle in a two dimensional current field is

$$\frac{dX_p}{dt} = U(X_p, t) \tag{2.1}$$

where X_p is the position of the particle and $U(x_p,t)$ is the velocity at the particle location. The time rate of change of the particle is dependent on the velocity at the position of the particle, however, the velocity field is not resolved to the same infinitely small resolution as theoretical particles. Velocities are averaged spatially. This averaging hides velocity perturbations smaller than the spatial average that can affect particle motion. On a molecular level, particle movement in a fluid is also subject to chaotic, irregular behavior. Robert Brown described this motion in 1826 when he observed irregular motion by colloidal sized particles in fluid. Einstein clarified this motion in 1905 when he determined that the irregular particle motion was caused by collisions with fluid molecules. The random movement of these particles, resulting in their dispersion is called Brownian motion. Particles in the ocean are experiencing random motion, similar to Brownian motion, due to small scale unresolved eddies and turbulence in the velocity field (Csanday, 1973). What is the importance of random walk due to small scale eddies?

Since after a time, t, the size of a cloud of particles will spread as:

$$\sigma \sim \sqrt{\kappa_H t} \tag{2.2}$$

where κ_H is the horizontal turbulent diffusivity, an effective length scale can be estimated. A typical small-scale eddy diffusivity of 100 m^2/s yields a spread of around 600 m after one hour. This length scale is smaller than the resolution of the hourly HF Radar velocity data, and only grows as $t^{1/2}$, while advection by strain and shear grows linearly with time, suggesting that random walk by small scale turbulence is not the dominant mode of particle separation.

Dispersion theory is usually broken down into two fields, absolute dispersion (single particle statistics) and relative dispersion (multiple particle statistics). In this study, the focus was on relative dispersion. Relative dispersion is usually estimated using particle pairs. For two particle statistics, relative dispersion is defined as the mean square pair separation at time t:

$$D^2(t) = \sum[(x_i(t) - x_j(t))^2 + (y_i(t) - y_j(t))^2] \tag{2.3}$$

Here, a form of relative pair dispersion, the Lagrangian Rate of Separation, was the main method used to estimate how particles were separating over time.

2.3 Lagrangian Rate of Separation

A method of quantifying particle separation rates is through a Lagrangian Rate of Separation (RoS) measurement, also know as a Lyapunov Exponent. For two particles dispersing exponentially over time, the Lagrangian RoS can be defined as:

$$\delta(t + \tau) = \delta(t)*e^{\lambda\tau} \tag{2.4}$$

where λ is the exponential rate of separation, t is the start time, τ is the final time, and δ is the position of the particle at time t or $t+\tau$. Two main variables are used to measure the Lagrangian RoS: distance and time. Depending on the intended use of the results, the Lagrangian RoS can be calculated with either time or space as the independent variable. When time is fixed, the Lagrangian RoS measures how far two particles separate over a fixed time. When space is fixed, the Lagrangian RoS measures how long it takes two particles to reach a specified distance. Due to the limited range of the HF Radar coverage area, time was fixed for all the calculations done here. The exponential rate of separation, with units time^{-1}, is simply a more specific way to measure relative dispersion. A positive Lagrangian RoS value represents two particles diverging over a fixed time, while a negative represents two particles converging over a fixed time.

The Lagrangian RoS is a useful tool for analyzing divergence and convergence in a velocity field, as well as mixing rates of particles, but it does not detail the kinematics of the velocity field that are responsible for the particle's movement, which is very important for many applications of Lagrangian studies. The Lagrangian RoS reduces a two dimensional velocity field into a one dimensional parameter, where direction is no longer important. Many applications reliant on surface current data, such as larval transport, marine pollution, and search and rescue operations, require direction dependence for accurate predictions. Since small scale turbulent diffusion processes have been neglected from this study, larger scale processes are responsible for particle separation rates.

2.4 Velocity Gradient Tensors

Another way to look at larger scale kinematics in a flow field is to examine the components of the velocity gradient tensor. The velocity gradient tensor is a means to quantify the kinematic properties of a velocity field responsible for the movement of passive particles. The components of a flow field are represented by the eigenvalues of the Jacobian of the velocity field (Olson, 2007). In order to understand the behavior of particles in a velocity field, it is useful to know what features in the velocity field are dominating and what direction those features will move a particle. Direction is harder to pinpoint due to the spatial averaging of the velocity field by the HF Radars, but identifying the velocity field kinematics responsible for certain dispersion patterns can be achieved using velocity gradient tensors. Velocity gradient tensor analysis can be used to supplement the Lagrangian RoS results.

Defining a stationary two dimensional flow field, as is commonly used in the study of surface ocean currents, with

$$\mathbf{U}(\mathbf{x}, t) = (u(x,y,t), v(x,y,t)) \tag{2.5}$$

the velocity can be expanded into a Taylor series near a point x_o. Discarding the higher order terms leaves

$$\mathbf{U}(\mathbf{x}, t) = \mathbf{U}_o + \mathbf{A}^*(\mathbf{x}(t)-\mathbf{x_o}(t)) \tag{2.6}$$

where $\mathbf{U}_o$ is the mean velocity, defined in this study by the spatial averaging of the HF radars, and $\mathbf{A}$ is the velocity gradient tensor.

$$\boldsymbol{A}_{\alpha\beta} = \begin{bmatrix} \frac{\partial u}{\partial x} & \frac{\partial u}{\partial y} \\ \frac{\partial v}{\partial x} & \frac{\partial v}{\partial y} \end{bmatrix} \tag{2.7}$$

To extract the properties of the flow, the velocity gradient tensor can be broken down into two main components: an antisymmetric part, representing vorticity, and a symmetric part, representing irrotational deformation (Batchelor, 1967). The antisymmetric part, $\zeta_{\alpha\beta}$ is one half of the difference between the velocity gradient tensor and its transpose:

$$\zeta_{\alpha\beta} = \frac{1}{2}\left(\boldsymbol{A}_{\alpha\beta} - \boldsymbol{A}_{\alpha\beta}\right) = \frac{1}{2}\begin{bmatrix} \frac{\partial u}{\partial x} & \frac{\partial u}{\partial y} \\ \frac{\partial v}{\partial x} & \frac{\partial v}{\partial y} \end{bmatrix} - \frac{1}{2}\begin{bmatrix} \frac{\partial u}{\partial x} & \frac{\partial v}{\partial x} \\ \frac{\partial u}{\partial y} & \frac{\partial v}{\partial y} \end{bmatrix} = \frac{1}{2}\begin{bmatrix} 0 & -\left(-\frac{\partial v}{\partial x} - \frac{\partial u}{\partial y}\right) \\ \left(\frac{\partial v}{\partial x} - \frac{\partial u}{\partial y}\right) & 0 \end{bmatrix} \tag{2.8}$$

with eigenvalues:

$$\lambda_{1,2} = \pm i\xi \tag{2.9}$$

The eigenvalues for the antisymmetric part of the velocity gradient tensor define relative vorticity and are imaginary. The flow is circular, trapping particles within the eddy. For an irrotational flow, $\xi = 0$.

The symmetric part of the velocity gradient tensor, $\eta_{\alpha\beta}$, representing irrotational deformation, is one half of the sum of the velocity gradient tensor and its transpose:

$$\eta_{\alpha\beta} = \frac{1}{2}\begin{bmatrix} \frac{\partial u}{\partial x} & \frac{\partial u}{\partial y} \\ \frac{\partial v}{\partial x} & \frac{\partial v}{\partial y} \end{bmatrix} + \frac{1}{2}\begin{bmatrix} \frac{\partial u}{\partial x} & \frac{\partial v}{\partial x} \\ \frac{\partial u}{\partial y} & \frac{\partial v}{\partial y} \end{bmatrix} = \begin{bmatrix} \frac{\partial u}{\partial x} & \frac{\frac{1}{2}\left(\frac{\partial u}{\partial y} + \frac{\partial v}{\partial x}\right)}{} \\ \frac{1}{2}\left(\frac{\partial v}{\partial x} + \frac{\partial u}{\partial y}\right) & \frac{\partial v}{\partial y} \end{bmatrix} \tag{2.10}$$

The symmetric part can be further decomposed into an isotropic divergence, Tr(η) and a non-divergent strain, $\eta'_{\alpha\beta}$. The isotropic divergence is simply

$$Tr(\eta) = \frac{\partial u}{\partial x} + \frac{\partial v}{\partial y} \tag{2.11}$$

while the non-divergent strain is defined as

$$\eta'_{\alpha\beta} = \eta_{\alpha\beta} - Tr(\eta)\delta_{\alpha\beta}/2 \tag{2.12}$$

$$\eta'_{\alpha\beta} = \begin{bmatrix} \frac{\partial u}{\partial x} & \frac{\frac{1}{2}\left(\frac{\partial u}{\partial y} + \frac{\partial v}{\partial x}\right)}{} \\ \frac{1}{2}\left(\frac{\partial v}{\partial x} + \frac{\partial u}{\partial y}\right) & \frac{\partial v}{\partial y} \end{bmatrix} - \begin{bmatrix} \frac{1}{2}\left(\frac{\partial u}{\partial x} + \frac{\partial v}{\partial y}\right) & 0 \\ 0 & \frac{1}{2}\left(\frac{\partial u}{\partial x} + \frac{\partial v}{\partial y}\right) \end{bmatrix} \tag{2.13}$$

$$\eta'_{\alpha\beta} = \frac{1}{2}\begin{bmatrix} \left(\frac{\partial u}{\partial x} - \frac{\partial v}{\partial y}\right) & \left(\frac{\partial u}{\partial y} + \frac{\partial v}{\partial x}\right) \\ \left(\frac{\partial v}{\partial x} + \frac{\partial u}{\partial y}\right) & -\left(\frac{\partial u}{\partial x} - \frac{\partial v}{\partial y}\right) \end{bmatrix} = \frac{1}{2}\begin{bmatrix} \sigma_1 & \sigma_2 \\ \sigma_2 & -\sigma_1 \end{bmatrix} \tag{2.14}$$

Since $\eta'_{\alpha\beta}$ is non-divergent, its trace is zero, and it represents non-divergent strain only. Solving for the eigenvalues of non-divergent strain:

$$\lambda_{1,2} = \pm 1/2(\sigma_1^2 + \sigma_2^2)^{1/2} \quad (2.15)$$

Since the eigenvalues are real, there can be stable or unstable nodes, or saddle points defining the flow (Olson, 2007). Complex eigenvalues also produce unstable and stable regions. An unstable region will have particles flowing outwards, with a stable region pulling particles towards the node. Knowing which eigenvalues dominate a flow field can assist in particle trajectory prediction.

The final decomposition is then:

$$A\alpha\beta = \xi\alpha\beta + \eta'\alpha\beta + Tr(\eta)\delta_{\alpha\beta}/2 \quad (2.16)$$

Computation of all the components of the velocity gradient tensor produces a more detailed analysis of ocean surface currents than by use of the Lagrangian RoS alone.

2.5 HF Radar data

The data used for this experiment was compiled from two HF radars deployed on the island of Oahu, Hawaii. One radar was deployed at Kaena Pt and the second radar was deployed at Koolina beach (Fig. 2). The radars were active from September 2002 until May 2003.

HF Radar coverage has a high spatial and temporal variability. Spatial coverage is usually better during day, but is highly dependent on the clarity of frequency used. Background noise, such as radio station frequencies, can interfere with radar coverage. In order to effectively look at dispersion, periods of relatively constant coverage were needed. Coverage variability for all four sites were reviewed and only periods where the coverage was adequately large for at least 24 hours were used for analysis.

The Lagrangian RoS was calculated by seeding the HF Radar derived velocity field with a gridded set of infinitely small particles. Particle trajectories were simulated using the HF Radar data by integrating

$$\frac{dX_p}{dt} = U(X_p, t) \tag{2.17}$$

using a fourth-order Runge-Kutta (RK4) integration method, where $U(x_p,t)$ is the bilinear interpretation HF radar velocity at the position of the simulated drifter. The HF radar velocity data used in these experiments was spatially averaged over a 2 km grid. Simulated drifters, deployed in grid formations and in clusters, the latter shown in Fig. 3, were released into the HF radar velocity field and advected for 100 hours. The gridded particles were set to be at a distance of 1 km apart and spaced to be in line with the HF Radar grid, yielding a dense field of particle trajectories (Fig. 4). After 1, 6, 12, 24, and 48 hours, the distance between adjacent particles was calculated and compared to the initial distance of 1km. In order to find regions of maximum stretching, each particles trajectory was compared to the particle initally to the north, south, east and west of its starting location. The particle pair resulting in the maximum separation distance was used in the Lagrangian RoS calculation. This process allowed areas that have significantly higher Lagrangian RoS values to be isolated.

The spatial extent of the HF Radar coverage varies greatly over the length of the radar deployment. The spatial coverage where valid Lagrangian RoS results are attained is always less than the spatial coverage of the HF Radar. Since the Lagrangian RoS is calculated from particle pairs over a set time, many particles will exit the HF Radar coverage area before the end of the calculation time. The Lagrangian RoS is not recorded for these locations. The speed at which the particles exit the coverage area is dependent on the strength of the current and the features in the velocity field, such as eddies, that would trap particles within the coverage area. Also, if the coverage of the radar reduces after the start of the integration, the smallest HF Radar coverage area will determine the maximum extent of Lagrangian RoS results.

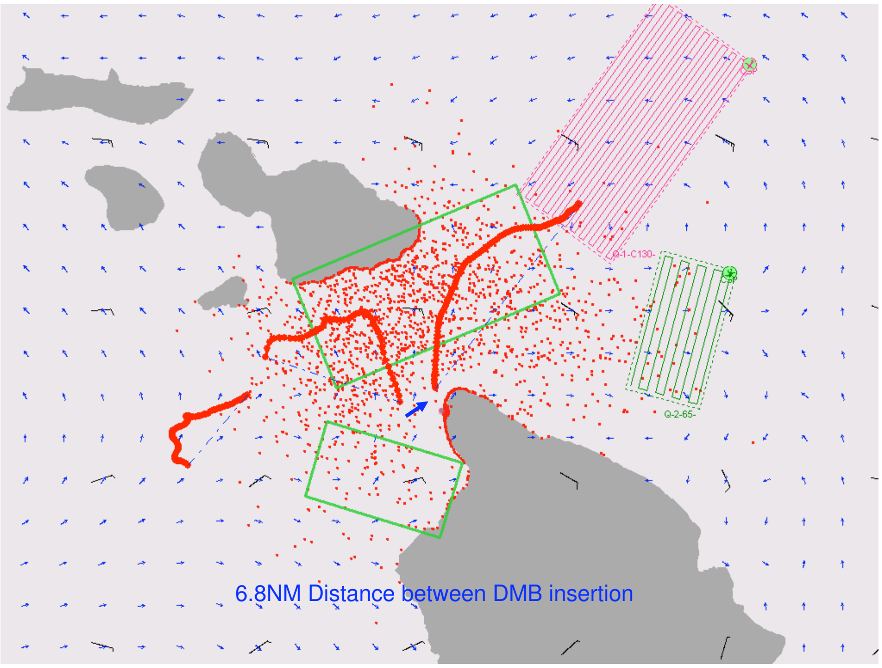

Fig 1: Search and Rescue case off Upolu Pt. Two SLDMB tracks from the USCG's deployment are shown in red. Even though they were launched near to each other, their tracks diverged 180 degrees.

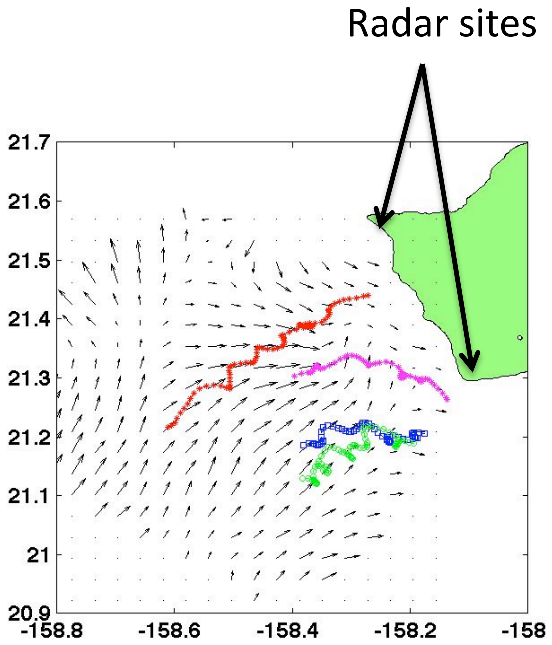

Fig 2: Locations of the two HF Radar sites, example total surface currents (black vectors) measured from the radars showing average spatial coverage, and four particle trajectories simulated using radar's currents.

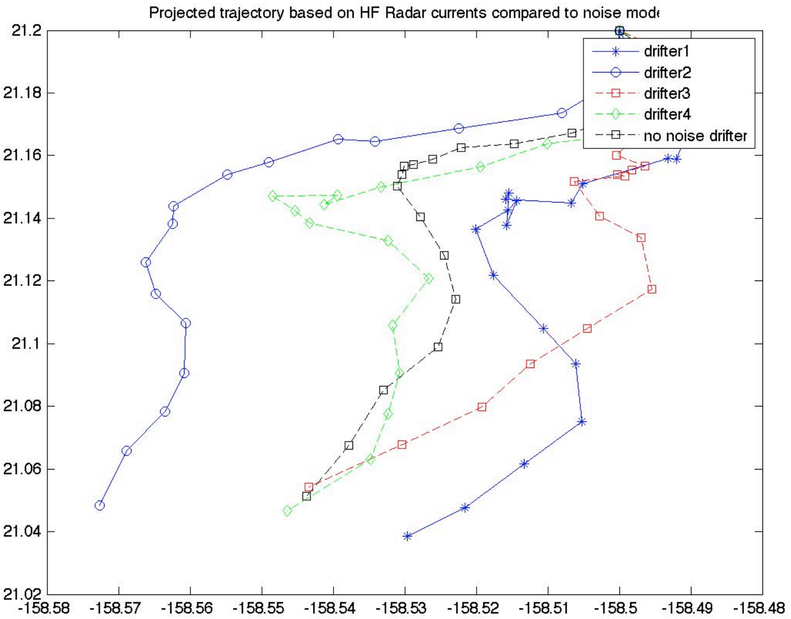

Fig 3: Example of a cluster of particles integrated using the HF Radar currents.

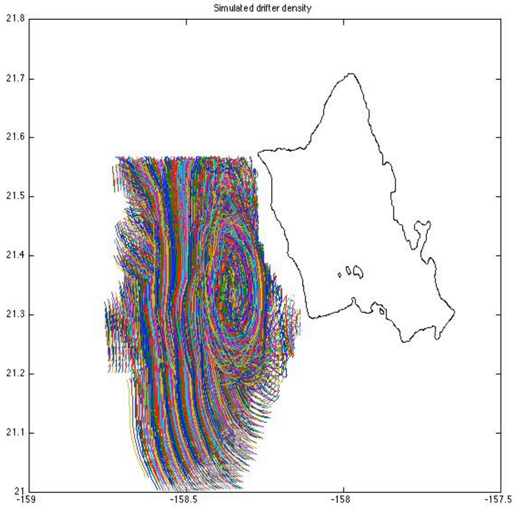

Fig 4: Example of the area covered by particle trajectories simulated using HF radar data.

Chapter 3

Defining an Instantaneous Rate of Separation

3.1 Introduction

As mentioned in Chapter 2, one of the basis' for the study of particle separation rates is the enhancement of Search and Rescue (SAR) operations. Between 1970 and 2006, the U.S. Coast Guard (USCG) averaged 52,602 SAR cases per year. Of those cases, over 95% occurred within 20 nautical miles of shore, well within range of HF Radars. Of all SAR cases, only 10% involve searches, with short searches (less than 24 hours) comprising 8%, and long searches (over 24 hours) comprising the remaining 2% of all SAR cases (COMDTINST M16130.2D, 2006). However the cases requiring searches, around 5,000 per year, cost the USCG over 50 million dollars annually (COMDTINST M16130.2D, 2006).

An unfortunate truth is that the condition of SAR victims degrades the longer they remain in distress, making the initial few hours of a SAR case very important. Since objects in the water are not stationary, understanding drift is very important for a successful SAR mission. Two key factors increase the likelihood a SAR victim will survive: effectively predicting where the person/object will drift, and decreasing the time required for an effective search. The Lagrangian RoS can be a useful tool for SAR operations if all the necessary variables are available. In order to pick up long term areas of convergence or divergence in a flow field, the Lagrangian RoS requires a long integration time. This is not always available to SAR coordinators. What is important is what is happening now. So the question becomes, how to get similar information from current data without a long integration period?

Here a new method for defining areas of convergence and divergence is explored, defined as an Instantaneous Rate of Separation (RoS). The Instantaneous RoS is derived from the components of the velocity gradient tensor, explained previously, in Chapter 2, and can be calculated directly from current data.

3.2 Instantaneous RoS: A Physical Understanding

Before delving into a complex derivation described in the next section, the equation for the Instantaneous RoS can be derived in a purely physical manner. Assuming particles in the flow field are infinitely small disregards the influence of wind on particle drift, leaving the velocity of the fluid at the location of the particle responsible for its movement. Random walk behavior and small scale diffusion processes can be disregarded as well, as the length scale of interest is significantly larger than that of random walk processes. Here, the kinematics of the fluid flow determine how the particle will move. In order to quantify an Instantaneous RoS, it is necessary to determine what flow features result in particles diverging, particles converging, and which ones have no influence at all. The most efficient way to do this is to use the components of the velocity gradient tensor.

As discussed in Chapter 2, the velocity gradient tensor can be broken down into three main components, an antisymmetric part representing vorticity, and a symmetric part which is comprised of an isotropic divergence portion and a non-divergent strain portion. It is the eigenvalues that determine flow behavior, the location of stagnation points, and the stability of nodes in the flow. Disregarding wind and small scale processes, the rate of particle separation must be a sum of the effects of the components of the velocity gradient tensor. Discussed in detail below, of the three main components of the velocity gradient tensor, only isotropic divergence and non-divergent strain work to separate two particles in a flow field.

In a purely rotational flow, shown in Fig. 5, the streamlines are concentric circles about the origin. This flow represents the antisymmetric portion of the velocity gradient tensor, or vorticity. Particles released into a purely rotational flow do not separate, but travel in circles about the origin. This behavior eliminates vorticity as a possible cause for particle separation.

Using the same method as in section 2, the symmetric part of the velocity gradient tensor is best broken down in an isotropic divergence and a non-divergent strain. Isotropic divergence, with eigenvalues, d, can be either positive or negative. Positive divergence represents particles separating, while negative values represent particles converging. Fig. 6 shows theoretical divergence and convergence fields. Isotropic divergence must be included as a cause for particle separation.

Non-divergent strain is another cause of particle separation. As demonstrated earlier, the eigenvalues for non-divergent strain are σ_1 and σ_2, (Fig. 7, Fig. 8 respectively). Particles released in a non-divergent strain velocity field will have very different paths depending on their initial location. From this discussion, it is easy to see why divergence and non-divergent strain were included in a definition for an Instantaneous RoS.

From the discussion above, it is easy to see that isotropic divergence and non-divergent strain are the main factors affecting the drift of particles in a velocity field. Therefore, the Instantaneous RoS must be a sum of the effects of divergence and strain:

$$\lambda_I = \sigma_o + d \tag{3.1}$$

where the Instantaneous RoS, λ_I, is equal to the eigenvalues for non-divergent strain, $\sigma_o = \sqrt{(\sigma_1^2 + \sigma_2^2)}$, plus the isotropic divergence, d.

3.3 Instantaneous RoS: A Mathematical Approach

Algebraically, the Lagrangian RoS cannot be simply related to the velocity gradient tensor. Starting with a velocity field as described by equation 2.9, consider the velocity field expanded into a Taylor series about a point x_o:

$$\frac{d\boldsymbol{x_1}}{dt} = \boldsymbol{U_o}(\boldsymbol{x_o}) + \boldsymbol{A}(\boldsymbol{x_o}) * (\boldsymbol{x_1} - \boldsymbol{x_o}) \tag{3.2}$$

As discussed by Flament et al. (2000) solutions for this set of equations depends on its eigenvalues. The resulting eigenvalues can be either real, imaginary, or complex and the solution for each case varies greatly. In order to relate the Lagrangian RoS to the velocity gradient tensor while retaining dependence on the impact of strain and divergence, another method must be used.

Assuming that the Lagrangian RoS is the rate of change of particle pair separation over time, an Instantaneous RoS can be calculated by using the limiting case of t=0 for the Lagrangian RoS. Starting with:

$$\frac{d}{dt}\left(\sqrt{(x - x_o)^2 + (y - y_o)^2}\right) = \boldsymbol{\lambda}\left(\sqrt{(x - x_o)^2 + (y - y_o)^2}\right) \tag{3.3}$$

where the Lagrangian RoS is acting as Instantaneous RoS. Expanding:

$$2(x-x_o)\frac{d(x-x_0)}{dt} + 2(y-y_o)\frac{d(y-y_0)}{dt} = 2\boldsymbol{\lambda}\left((x-x_o)^2+(y-y_o)^2\right)$$

(3.4)

If the time derivatives of (x-x_o) and (y-y_o) are, as derived from the original definition of the velocity gradient tensor equation, respectively

$$\frac{d(x-x_o)}{dt} = \frac{\partial u}{\partial x}(x-x_o) + \frac{\partial u}{\partial y}(y-y_o)$$

(3.5)

$$\frac{d(y-y_o)}{dt} = \frac{\partial v}{\partial x}(x-x_o) + \frac{\partial v}{\partial y}(y-y_o)$$

(3.6)

then replacing the time derivatives of (x-x_o) and (y-y_o) with 3.5 and 3.6 gives the equation:

$$(x-x_o)^2\frac{\partial u}{\partial x} + (x-x_o)(y-y_o)\left[\frac{\partial u}{\partial y}+\frac{\partial v}{\partial x}\right] + (y-y_o)^2\frac{\partial v}{\partial y} = \boldsymbol{\lambda}\left((x-x_o)^2+(y-y_o)^2\right)$$

(3.7)

Substituting in the relationships for σ_1, σ_2, and d (defined in Chapter 2)

$$\frac{\partial u}{\partial x} = \sigma_1 + d, \frac{\partial u}{\partial y} + \frac{\partial v}{\partial x} = \sigma_2, and\ \frac{\partial v}{\partial y} = d - \sigma_1$$

(3.8)

gives an equation for the relationship between the Rate of Separation and the velocity gradient tensor components:

$$(x-x_0)^2[\sigma_1+d] + 2(x-x_o)(y-y_o)[\sigma_2] + (y-y_o)^2[d-\sigma_1] = \boldsymbol{\lambda}\left((x-x_o)^2+(y-y_o)^2\right)$$

(3.9)

The antisymmetric portion of the velocity gradient tensor is not represented in this relationship, because only the strain and divergence are responsible for particle pair separation. The relationship between divergence, strain and the Rate of Separation is not immediately apparent from the form of equation 3.9. To simplify this, trigonometric identities can reduce the equation to:

$$\lambda_o = \sigma_1 * \cos 2\theta + \sigma_2 * \sin 2\theta + d \qquad (3.10)$$

where θ is the angle between the two types of strain, σ_1 and σ_2. To simplify this further into a usable entity, it is best to take a more visual approach to understand what σ_1 and σ_2 represent. Figure 7 and Fig. 8 show the velocity field produced from theoretical σ_1 and σ_2 fields, respectively. From this figure, it is evident that these fields are defined merely from their angle of rotation off the primary axis'. The dependence on the angle of rotation, φ, can be eliminated by relating σ_1 and σ_2 to a generic strain term, σ_o.

$$\sigma_1 = \sigma_o \cos(2\varphi) \qquad \sigma_2 = \sigma_o \sin(2\varphi) \qquad (3.11)$$

Now solving for σ_o yields:

$$\sigma_o = \sqrt{(\sigma_1^2 + \sigma_2^2)} \qquad (3.12)$$

which is simply the total strain. Replacing σ_1 and σ_2 with equations 3.17 gives a final relationship:

$$\lambda = \sigma_o + d \qquad (3.13)$$

which is a much simpler form of equation 3.9. This shows that for an instantaneous moment in a velocity field, particle separation is dependent on the total strain rate and the divergence of the flow field. There is now a definition for a Lagrangian RoS (λ_L) based on the relative dispersion of particle pairs over a fixed time, and an Instantaneous RoS (λ_I) based on the rate of strain and divergence in a flow field, representing the zero order Lagrangian RoS at t=0. The Instantaneous RoS can be calculated immediately from current data available, without having to rely on time-dependent integrations.

3.4 A Comparison between Lagrangian and Instantaneous RoS

Both the Lagrangian RoS and Instantaneous RoS were calculated hourly from the HF radar current data. Both were normalized by the Coriolis parameter and are shown in units of *f*. The Lagrangian RoS measures particle separation rates. The longer the fixed time used in the calculation, the more features the Lagrangian RoS is able to pick up. For the HF Radar data off Oahu, a 12 hour and 6 hour fixed times yielded the most robust results.

A correlation is not immediately apparent in a side by side comparison of the two variables, a 6 or 12 hour fixed time Lagrangian RoS and the corresponding Instantaneous RoS. An example, on October 14, 2002 at 0200,. the six hour fixed time Lagrangian RoS results (Fig. 9) do not match the Instantaneous RoS results (Fig 10). This discrepancy is due to the way the Lagrangian RoS is calculated. The Lagrangian RoS is calculated by integrating forward in time. The features in the flow field responsible for separating two particles can occur anytime during the integration, but the results are applied to the time the integration was started. This gives an inherent lag in any correlation between the Instantaneous RoS and the Lagrangian RoS. A comparison of the 6 hour fixed time Lagrangian RoS results for October 14, 2002 at 0200 and Instantaneous RoS results for October 14, 2002 at 0400 yields closer results (Fig. 11). Here, some of the dominant features in the Lagrangian RoS results begin to show up in the Instantaneous RoS results. This indicates that the features responsible for causing the greatest separation during the Lagrangian RoS calculations occurred 2 hours after the integration process began. The lag is not consistent throughout the study. During periods where the flow is nearly steady, without eddy activity, fronts, or other features, the Lagrangian RoS and Instantaneous RoS results compare well directly. The lag depends on when the integration was started and how long it takes a feature to develop in the flow field. So, the Instantaneous RoS acts as an instantaneous guide to how particles will react, while the Lagrangian RoS picks out features in the flow field that dominate over longer time periods.

A better way to compare would to be use a Lagrangian RoS computation using a 1 hour fixed time. This would be the closest result to the Instantaneous RoS. Here the correlation becomes much better. The 1 hour fixed time Lagrangian RoS (Fig. 12) for the same time period used early, October 14, 2002 at 0200, matched the spatial patterns of the Instantaneous RoS. Using a regression analysis, the correlation between the 1 hour Lagrangian RoS and the Instantaneous RoS had an R^2 value of 0.8 (Fig. 13), indicating a strong correlation. A regression between the 6 hour and 12 hour Lagrangian RoS and Instantaneous RoS yielded much poorer results of $R^2 = 0.107$ and $R^2 = 0.009$, respectively (Fig. 14, Fig. 15). A plot of correlation versus time shows an almost exponential decline in correlation over time (Fig. 16).

This exponential decrease in correlation between the 1-hour Lagrangian RoS and Instantaneous RoS has strong implications for dispersion applications such as SAR and marine pollution response. The flow on the west side of Oahu was not steady during the study, but varied greatly with time. This variation indicates that using time averages of the flow to predict particle motion or to determine regions of convergence or divergence, is not a reliable method. For a steady flow, the Instantaneous RoS and Lagrangian RoS should correlate well, indicating that regions of divergence and convergence will be similar over time. However, here, after only 6 hours, the flow had changed so greatly, that regions of strong convergence became regions of divergence. An operator conducting marine pollution missions or search and rescue in the vicinity of Oahu will need to be vigilant in keeping up with the changing velocity fields.

Another noteworthy difference in the Lagrangian RoS and Instantaneous RoS calculations is the spatial coverage of each variable. The Instantaneous RoS is calculated directly from the velocity field itself, whereas the Lagrangian RoS field is calculated by seeding the flow field with particles and integrating over time. Due to the limited spatial nature of HF radar data, after a day, not many particles remain the the radar coverage area. Once the particle exits the HF radar coverage area, it is no longer used in the calculation, reducing the available data points. For any Lagrangian RoS calculation longer than 1 hour, this reduces the amount of usable results. Fig. 17 shows a comparison of the 12 hour Lagrangian RoS results and Instantaneous RoS results for an hour before midnight on October 14, 2002. The Instantaneous RoS results covered a greater area than the 12 hour Lagrangian RoS results, due to a HF Radar coverage reduction during the integration period.

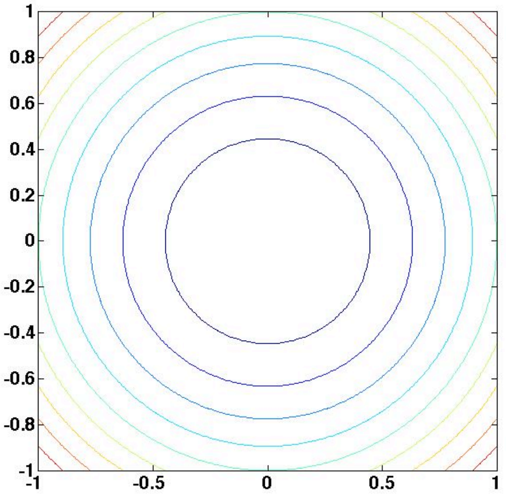

Fig. 5: Streamlines for the anti-symmetric portion of the velocity gradient tensor, representing vorticity.

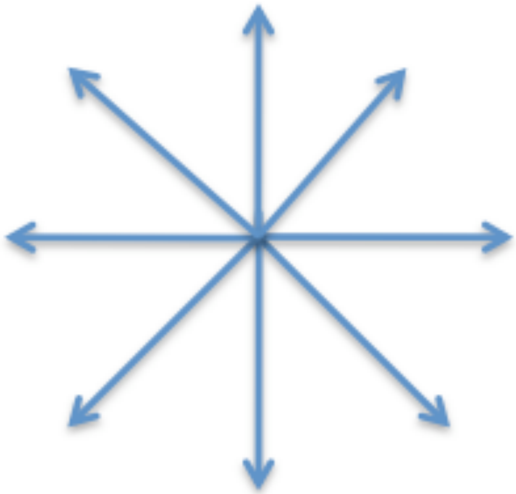

Fig. 6: Theoretical divergence field. Pure convergence would be in the reverse direction, will flow going into the node.

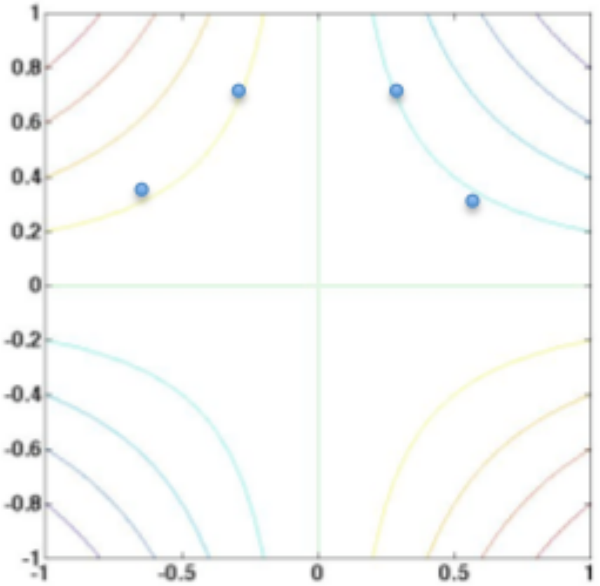

Fig. 7: Streamlines for one component of strain, σ_1. Blue dots represent particles following the streamlines.

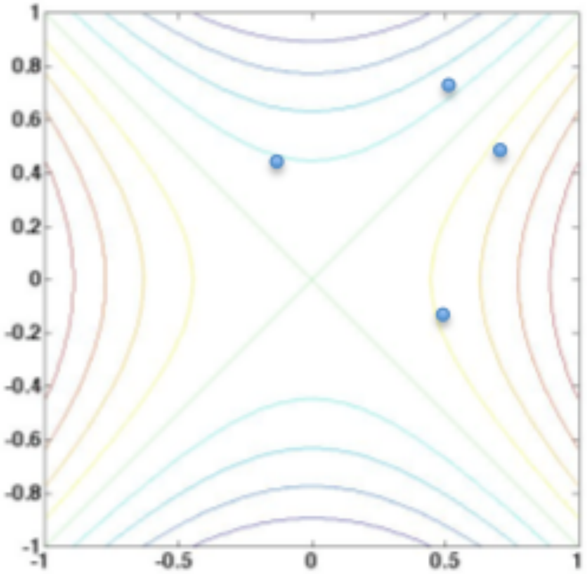

Fig. 8: Streamlines for the second component of strain, σ_2. Blue dots represent particles following the streamlines.

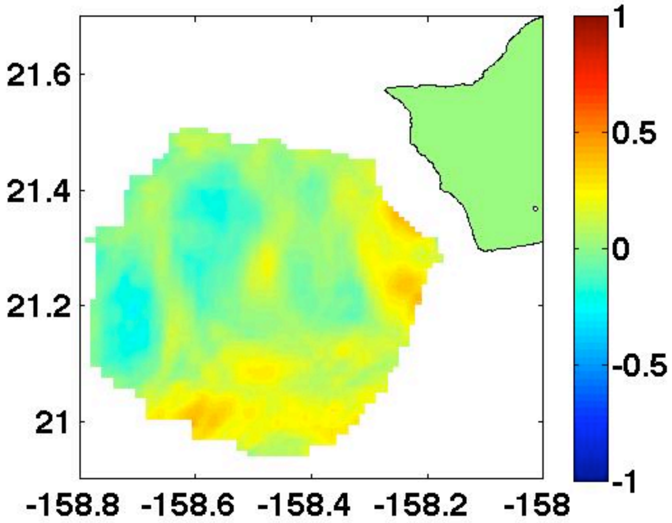

Fig. 9:The 6 hour Lagrangian RoS for October 14, 2002 at 0200. The Lagrangian RoS (in 1/s) has been normalized by the Coriolis parameter.

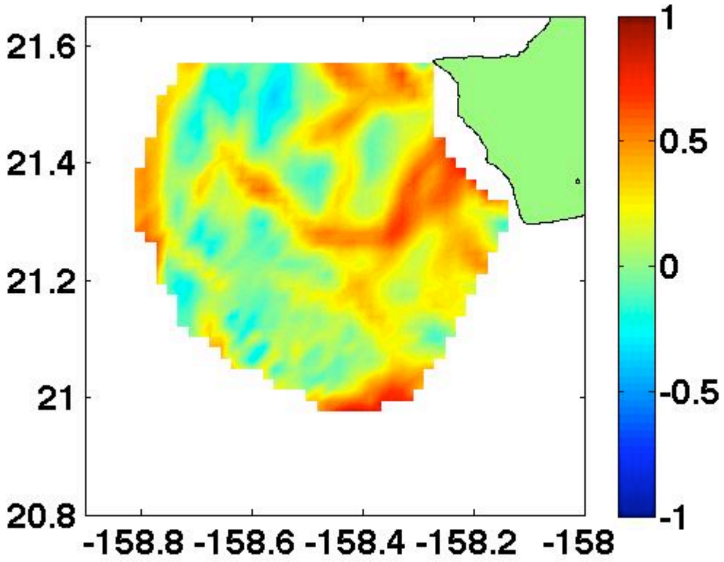

Fig. 10: The Instantaneous RoS for October 14, 2002 at 0200. The Instantaneous RoS (in 1/s) has been normalized by the Coriolis parameter.

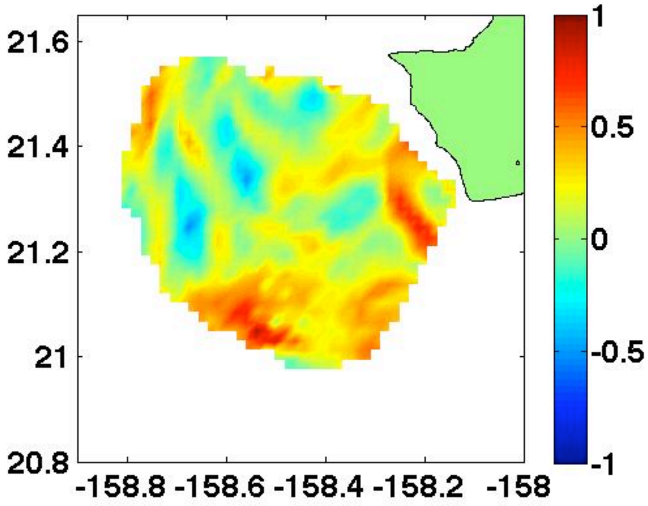

Fig. 11: Instantaneous RoS results for October 14, 2002 at 0400. The Instantaneous RoS (in 1/s) has been normalized by the Coriolis parameter.

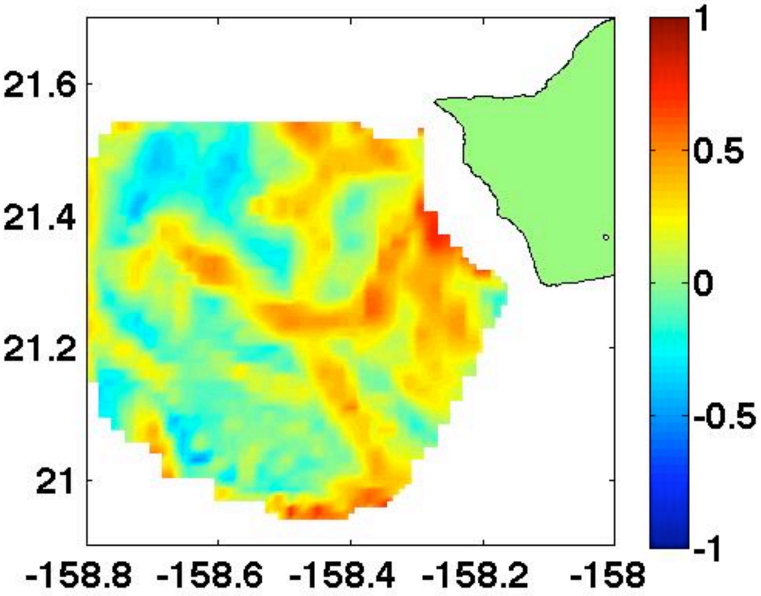

Fig. 13: 1 hour fixed time Lagrangian RoS for October 14, 2002 at 0200. The Lagrangian RoS (in 1/s) has been normalized by the Coriolis parameter

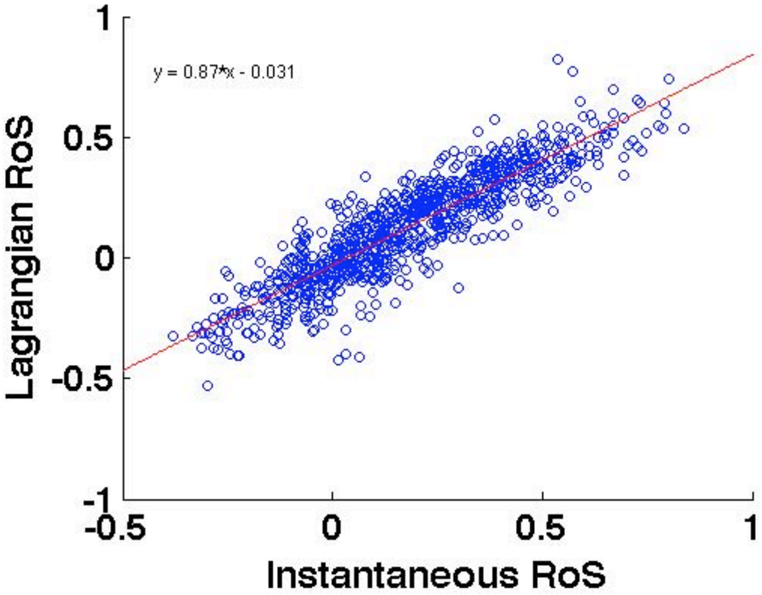

Fig. 13: Scatter plot of the 1 hour fixed time Lagrangian RoS versus the Instantaneous RoS for October 14, 2002 at 0200. Both the Lagrangian RoS and Instantaneous RoS are shown here normalized by the Coriolis parameter.

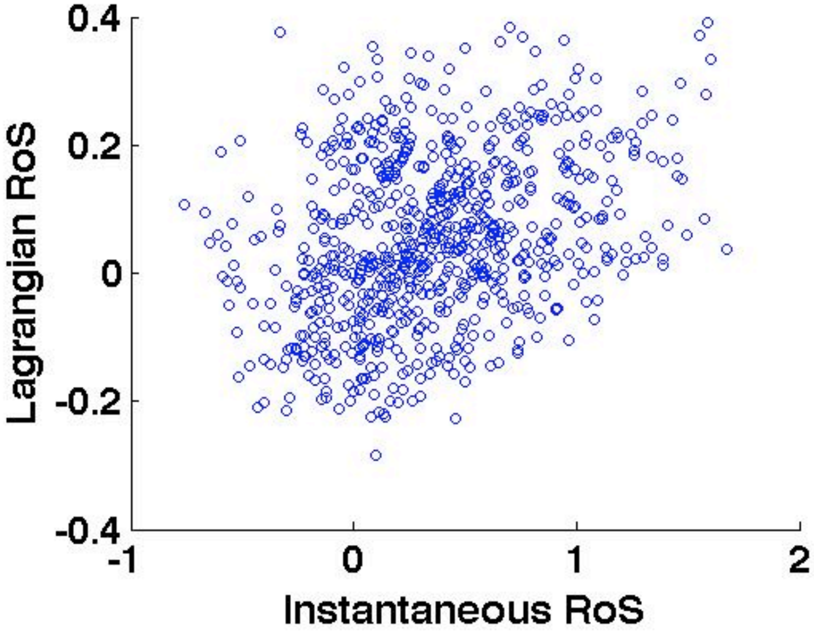

Fig. 14: Scatter plot of the 6 hour fixed time Lagrangian RoS versus the Instantaneous RoS for October 14, 2002 at 0200. Both the Lagrangian RoS and Instantaneous RoS are shown here normalized by the Coriolis parameter.

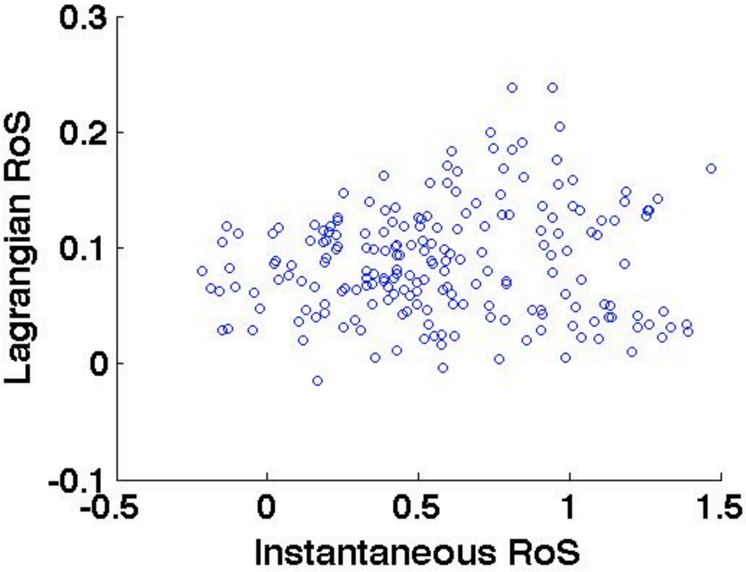

Fig. 15: Scatter plot of the 12 hour fixed time Lagrangian RoS versus the Instantaneous RoS for October 14, 2002 at 0200. Both the Lagrangian RoS and Instantaneous RoS are shown here normalized by the Coriolis parameter.

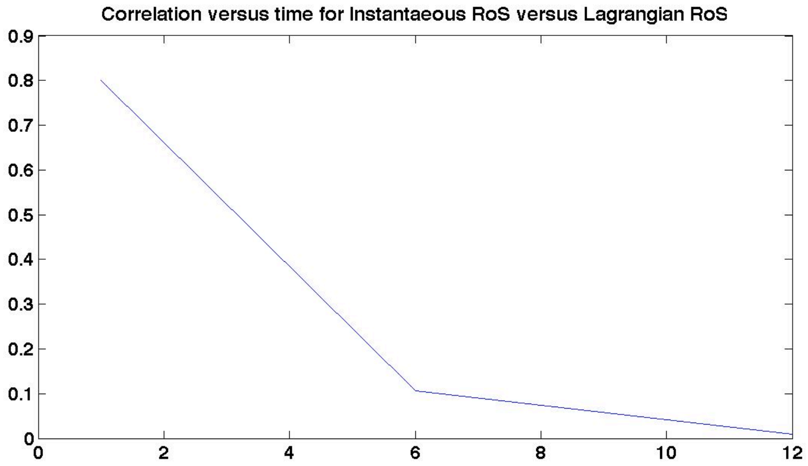

Fig. 16: Correlation of the Lagrangian RoS and Instantaneous RoS versus time (in hours) for October 14, 2002.

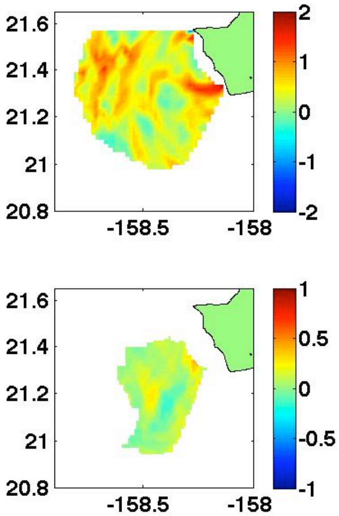

Fig. 17: Top: Instantaneous RoS for October 14, 2002 at 2300. Bottom: 12 hour Lagrangian RoS for the same time period, showing a drastic reduction in coverage. Both the Lagrangian RoS and Instantaneous RoS are shown here normalized by the Coriolis parameter.

Chapter 4

Using Rates of Separation to Describe General Properties of the Flow

4.1 Introduction

The Lagrangian RoS and the Instantaneous RoS can both be used to examine flow features. Here, general properties of the flow are discussed, including seasonal trends. Followed by a discussion on how the Lagrangian and Instantaneous RoS are applied to the HF Radar data to pick out unique features in the flow that can aid a SAR case.

4.2 Dynamics in the lee of an island

The mesoscale flow around an oceanic island is drastically affected by the rapid changes in bathymetry and topography. Large-scale currents are subject to instabilities as they cross paths with an island, resulting in an enhanced eddy field on the leeward side (Lumpkin et al, 2000). Atmospheric flow is also affected by land topography. Changes in topography result in variations in wind stress curl, leading to changes in Ekman pumping and eddy formation (Chavanne et al, 2002). The island of Oahu is a member of the Hawaiian Archipelago, located in the middle of the Pacific subtropical gyre. Due to their location, the islands of Hawaii are in the path of the North Equatorial Current (NEC) and are subject to steady northeast trade winds over most of the year. The interruption of the mean wind and current field by the Hawaiian Islands causes strong eddy fields in the lee of the islands (Chavanne et al, 2002).

Island effects and the resulting eddy field are more commonly studied on the island of Hawaii, due to its larger size and dynamic topography. However, the island of Oahu can still exhibits wind shear patterns (Fig 18) consistent with the theoretical island dynamics outlined above. The dynamics resulting from Oahu blocking both current and wind patterns should result in a region of divergence in the Northern lee area off Oahu (Fig. 19). Using the 12 hour Lagrangain RoS, regions of relatively strong divergence can be seen in the Northern section of the HF Radar field (Fig. 20). Similar features can be seen in the Instantaneous RoS, an extreme example is September 27, 2002 at 1300 (Fig. 21), where a large divergence patch exist around the latitude of the Northwestern edge of Oahu. These regions of divergence are in the area expected, but island dynamics is just one possible reasonable explanation. Without higher resolution wind data for the corresponding time period, it is impossible to say with certainty.

4.3 General Dispersion Statistics

The HF Radar data used in this study was computed hourly and at a spatial resolution of 2km. The data was broken up into two main periods: fall and spring. The fall data extends from September 6, 2002 until November 16, 2002. The spring data extends from March 4, 2003 until April 29, 2003. The distribution of zonal and meridional HF radar velocities for one day are shown in Fig. 22 and Fig. 23. Both zonal and meridional velocities exhibit Gaussian like distribution, however the meridional velocity distribution shows a mean wind speed of 15 cm/s while the zonal distribution is centered around 0 cm/s. The distribution did not vary from its Gaussian like form during the study. The average direction of the flow past Oahu changed both daily and seasonally. The daily averaged current direction measured by the HF radar for fall and spring (Fig. 24) varied greatly. The average current direction was more variable in the fall. The spring data had a more persistent average current direction to the NorthEast. Hourly averaged current directions for the fall period (Fig. 25) show a noticeable diurnal pattern emerging. Diurnal patterns are also apparent in the spring data (Fig. 26), but the direction remains consistent even at the hourly scale.

Every hour, 5,616 virtual particles were seeded into the total currents produced by the HF radars on Oahu. The area seeded by particles was created to be larger than the average HF radar coverage. This accounted for fluctuations in HF radar coverage. Disregarding those particle trajectories that remained in the HF radar coverage less than five hours (those lying on the outskirts of the grid), the average time the particles remained in the flow was 29 hours. The time it took a particle to exit the HF radar coverage area varied greatly over the length of the study. Particle retention was highest during the end of an eddy event when the average time particles remained in the coverage area was 48 hours. Particle retention was lowest during the spring period, when the time dropped to 25 hours in the HF radar coverage, with some daily averages reaching as low as 18 hours. Fig. 27 shows histograms of how many particles exited the HF radar coverage area during each hour for the fall period. The first histogram, Fig. 27a, shows particle exit times for September 23, 2002, with an average time of 26 hours. The second histogram, Fig. 27b, shows particle exit times for October 14, 2002 a week before an eddy developed in the lee of Oahu, with an average retention time of 24 hours. The next histogram, Fig. 27c, shows particle exit times for October 26, 2002, during an anticyclonic eddy, with an average time of 37 hours. The last histogram, Fig. 27d, shows exit time for November 3, 2002, during the anticyclonic eddy's break-up, with an average retention time of 48 hours. Fig 28 is a histogram depicting particle exit time on March 30, 2003, during the spring HF Radar data. The average particle retention time was 24 hours for March 30, 2002.

Absolute dispersion as a function of time was calculated for each initiation of particle integration. Fig. 29, is a logarithmic plot of absolute dispersion, A^2, versus time in hours. Plotted alongside is a squared dependence on time, representing Ballistic dispersion and a linear dependence on time, representing Fickian dispersion. The absolute dispersion calculated from the HF radar data most closely resembles Ballistic dispersion. Ballistic dispersion is characteristically found at small times, as those used here.

4.4 Long term patterns

Both the Instantaneous RoS and the Lagrangian RoS varied greatly over time, but long term averages revealed some interesting patterns. Fig 30 is a three month time average of the Instantaneous RoS from September through November using the total currents produced from the HF Radar. Immediately apparent is the dominance of small scale features, even over a three month time average. By comparison, the three month Instantaneous RoS fall average using currents where the tides have been removed (Fig 31) is not dominated by small scale features. Instead, a region of particle convergence is dominant in the direct lee of Oahu, with a region of particle divergence to the North. The sharp contrast between average Instantaneous RoS values calculated with total currents versus those calculated without tides highlights the importance of tides in predicting particle separation rates.

The three month average Instantaneous RoS for fall using currents with tides removed showed a general region of particle divergence on the Northern edge of the HF Radar field and a region of particle convergence below. This general pattern agrees with the divergence, d, calculated directly from the HF Radar currents without tides (Fig 32). These regions of dominant particle separation and particle convergence are most likely due to the wind shear patterns in the lee of Oahu (Fig 18). As the wind reaches Oahu, the land mass impedes its flow creating shear patterns on the leeward side of the island. These wind shears cause transport in the surface layer and the resulting regions of convergence and divergence.

The time averages varied between fall and spring. In spring, the three month average Instantaneous RoS for total currents was still dominated by small scale features, indicating tides were still an important feature, regardless of season. However, the wind-induced convergence zone in the lee of Oahu was more prominent in the fall period than during the spring period. In the spring, there was no region of dominant convergence (Fig 33). There was still a region of stronger particle separation near the northern limits of the HF Radar, but the region in the lee had smaller positive values close to zero, indicating, on average, particles did not separate noticeably. This difference could be due to seasonal changes in wind patterns or winds that disrupted the dominant northeast trade winds, causing a shift in surface currents around the island. The average direction of the surface currents in the spring were to the north (Fig 34) whereas in the fall, the average direction was to the northeast, but varied more close to shore (Fig 35). The currents in the spring were also less varied than in the fall period.

4.5 Practical Applications

To discuss a practical application of the Instantaneous RoS, let us return to our example of the lost kayaker on the island of Hawaii. If HF Radars had been in place near Upolu Pt. when the kayaker became lost, they would have been useful in helping predict the correct drift pattern. Because the surface currents diverged so quickly directly off the point, the resulting search are was expanded. The higher resolution surface currents provided by HF Radars would have helped narrow the search area by helping identify the exact region where the surface currents diverged. Based upon the trajectories of the two SLDMBs deployed in area the kayaker was last seen, it appears there was a region of heavy strain. The Instantaneous RoS would have been able to identify the regions of highest strain and therefore the regions of highest particle separation. Although just a snapshot, monitoring the changes in the Instantaneous RoS would have helped identify the position of the surface current divergence. Knowing the current structure resembled a strain would have helped rescuers decide where to search and where to place SLDMBs.

Another more directly related application is the containment of marine pollution. The Instantaneous RoS provides a surface map of regions of convergence and divergence. Tracking these regions over time could be used to help estimate the possible extent of a marine spill. If a region of convergence exists near a coastline, it could lead responders to set up equipment onshore where the pollution was expected to collect.

Both of these applications of the Instantaneous RoS have potential to positively impact incident first responders. Further research into the applicability of the Instantaneous RoS to search and rescue as well as marine pollution response is needed, including possible integration into the U.S. Coast Guard's search and rescue computer program, SAROPS.

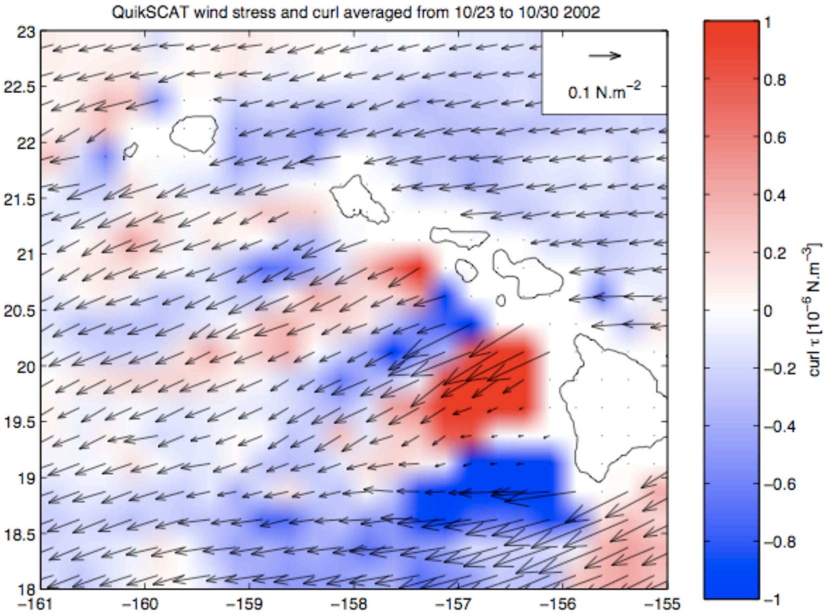

Fig. 18: Wind stress vectors and curl from QuikSCAT at 25km resolution, averaged from October 23 to 30, 2002 (from Chavanne, 2007)

.

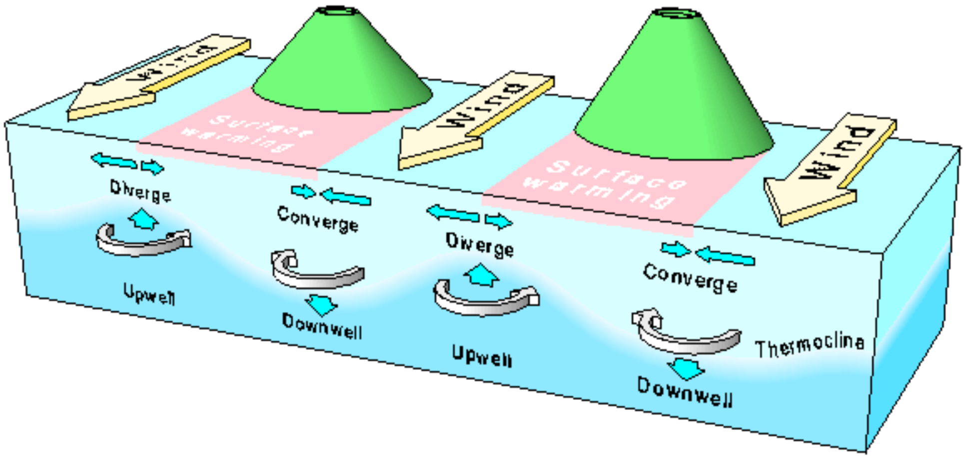

Fig. 19: A cartoon showing the resulting island dynamics due to blocking wind and current patterns, showing regions of divergence and convergence in the lee of the island. From Ocean Atlas of Hawaii (Flament, 1996).

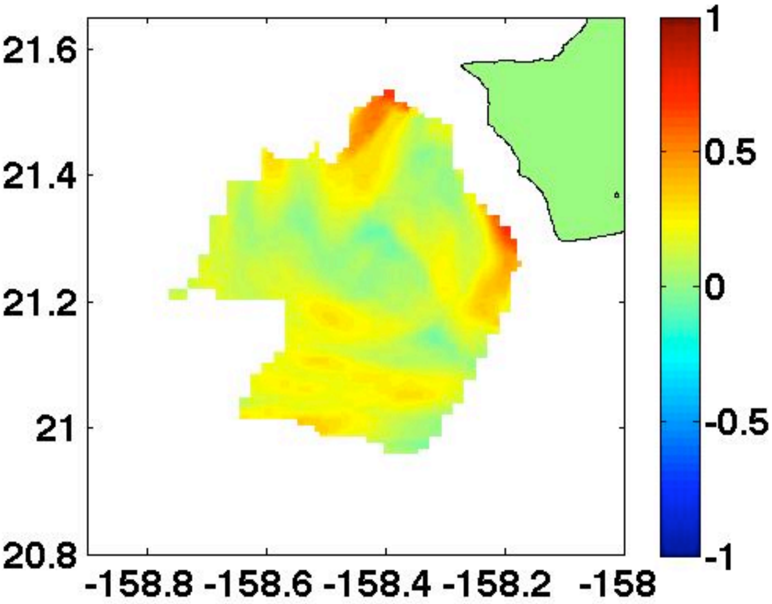

Fig. 20: 12 hour Lagrangian RoS showing region of moderate divergence stemming from the northwest corner of Oahu. The Lagrangian RoS (in 1/s) has been normalized by the Coriolis parameter.

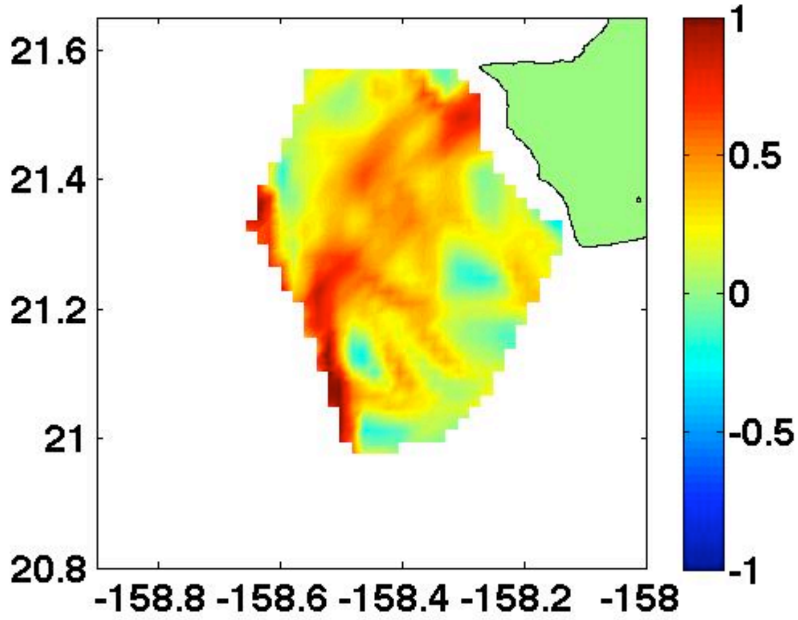

Fig. 21: Instantaneous RoS for September 27, 2002 at 1300 showing the region of strong divergence stemming from the northwest corner of Oahu. The Instantaneous RoS (in 1/s) has been normalized by the Coriolis parameter.

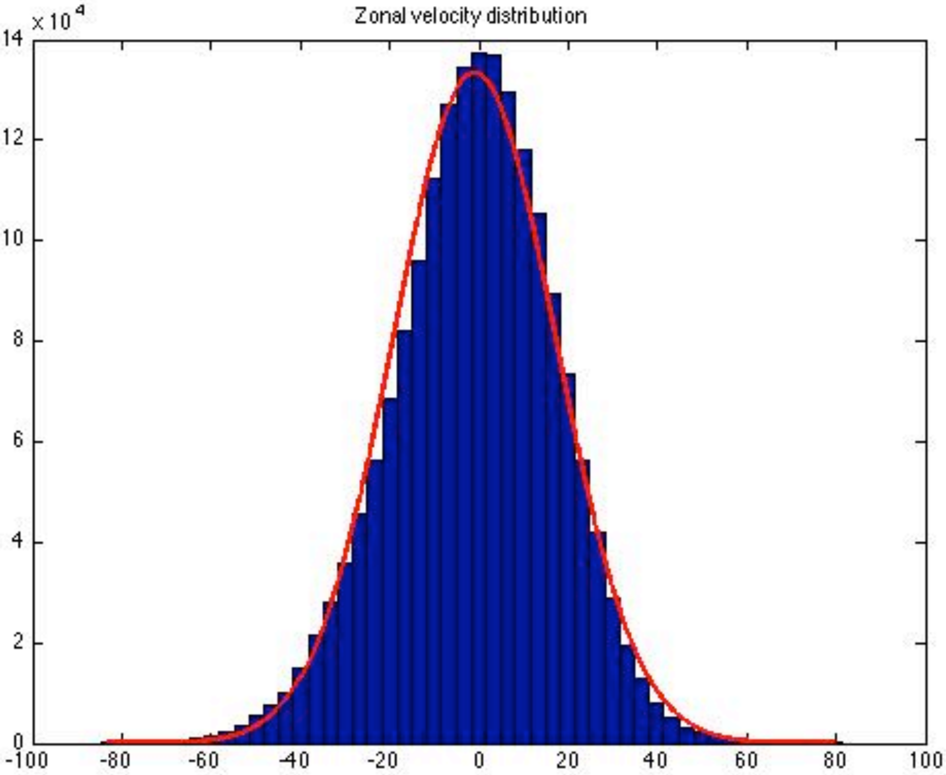

Fig. 22: Zonal current distribution, in cm/s.

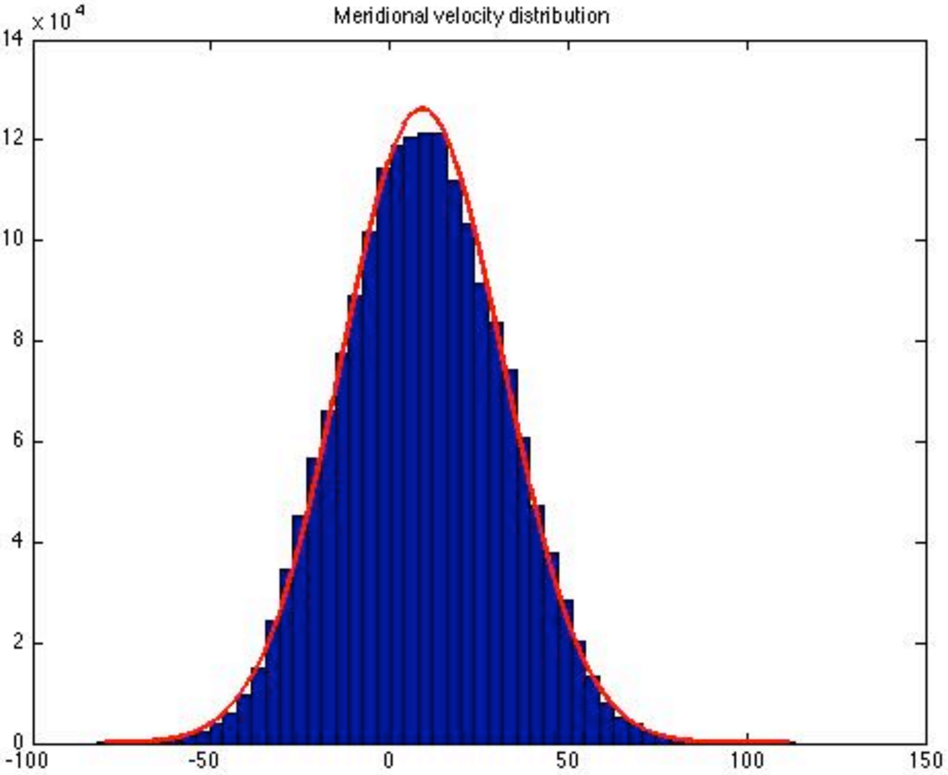

Fig. 23: Meridional velocity distribution, in cm/s.

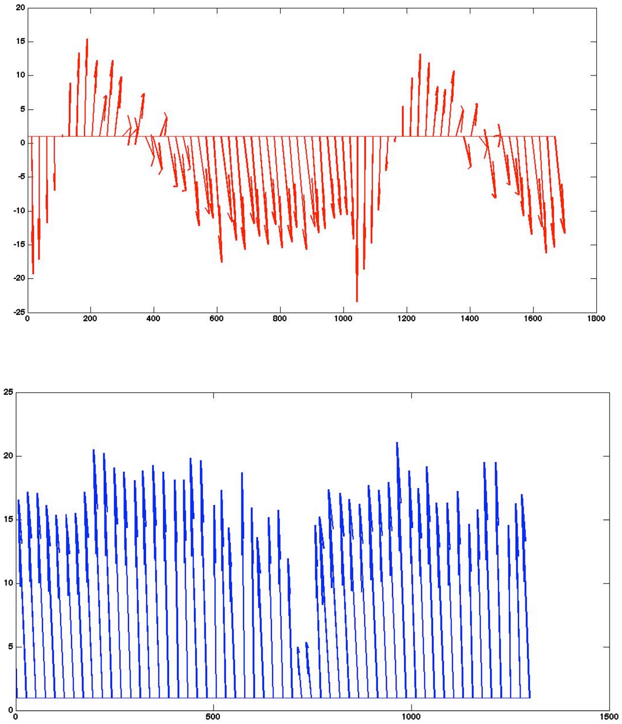

Fig. 24: Top: Fall daily averaged current direction. Bottom: Spring daily averaged current direction. Time is shown in hours. Current velocities are shown in cm/s

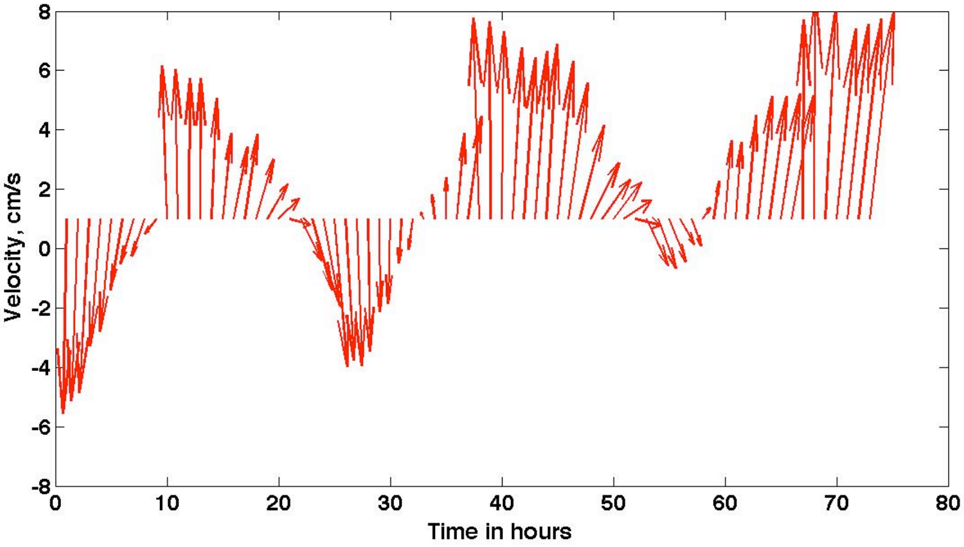

Fig. 25: Hourly averaged currents over three days for fall

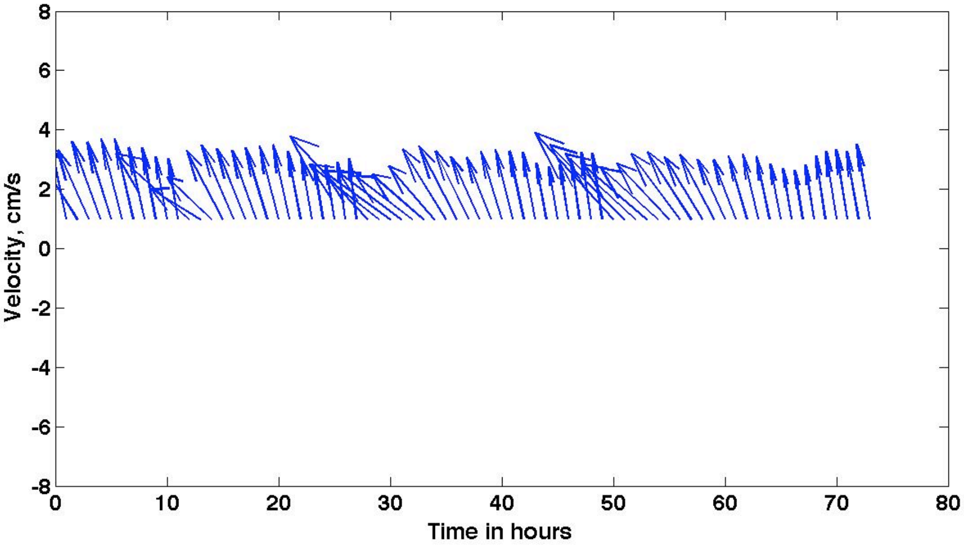

Fig. 26: Hourly averaged currents for three days during spring.

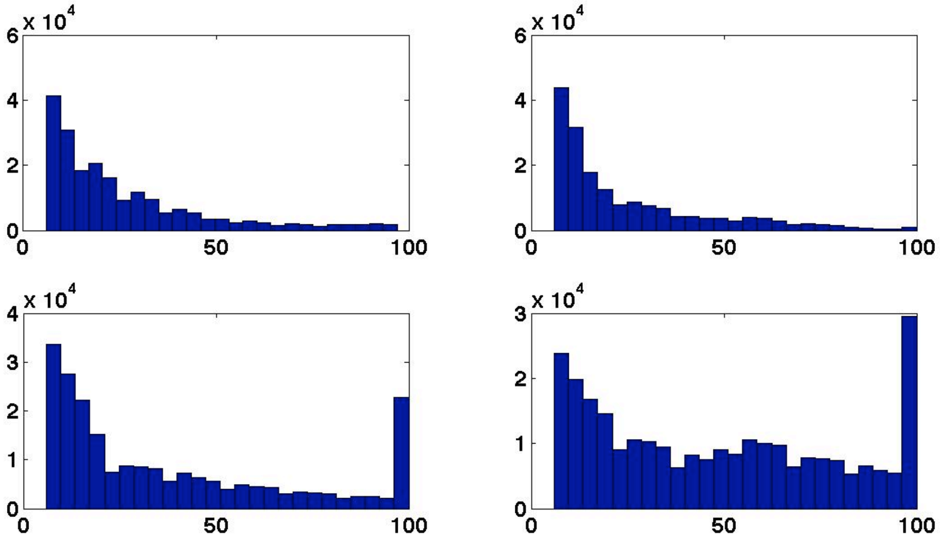

Fig 27: Histogram depicting how many particles exited the HF Radar coverage area at each hour of integration. Top Left: For an integration started on September 23, 2002. Top Right: For an integration started on October 14, 2002. Bottom Left: for an integration started on October 26, 2002. Bottom Right: for an integration started on November 3, 2002.

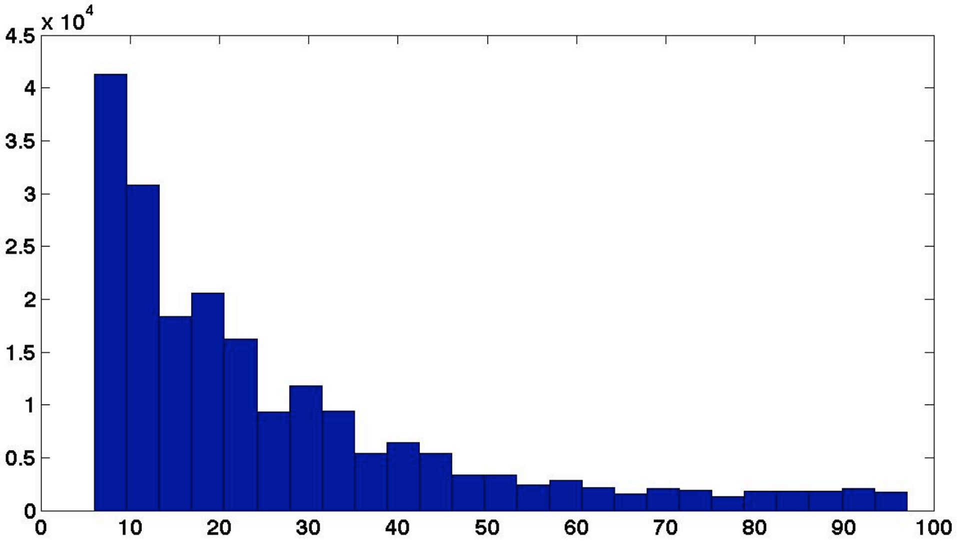

Fig. 28: Histogram depicting number of particles remaining in HF Radar coverage every hour for an integration started on March 30, 2003.

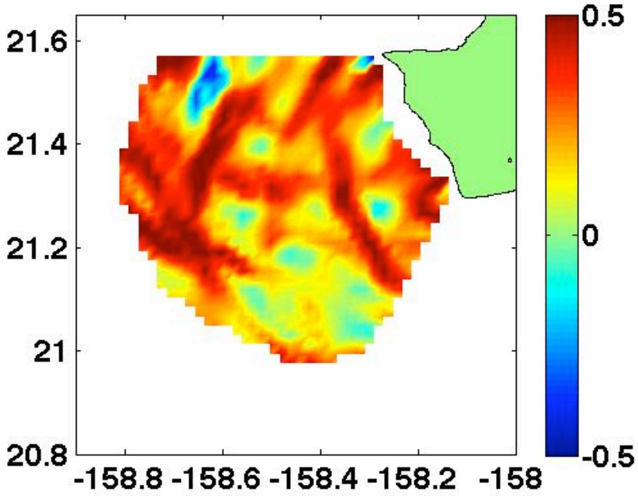

Fig. 30: Three month averaged Instantaneous RoS for September through November, 2002 using total currents. Instantaneous RoS (1/s) shown here normalized by Coriolis parameter.

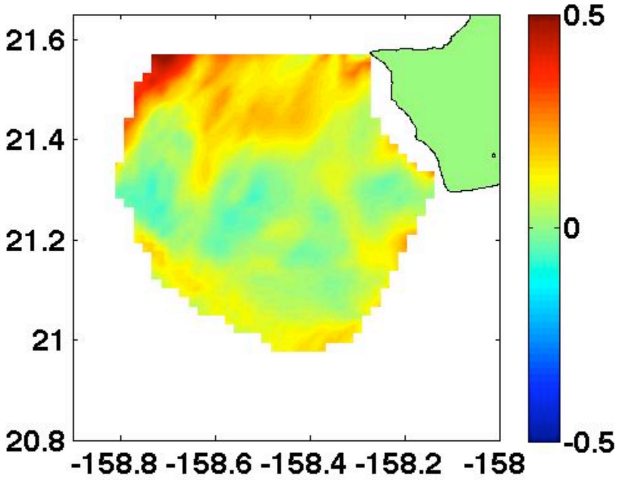

Fig. 31: Three month averaged Instantaneous RoS for September through November, 2002 using detided currents. Instantaneous RoS (1/s) shown here normalized by Coriolis parameter.

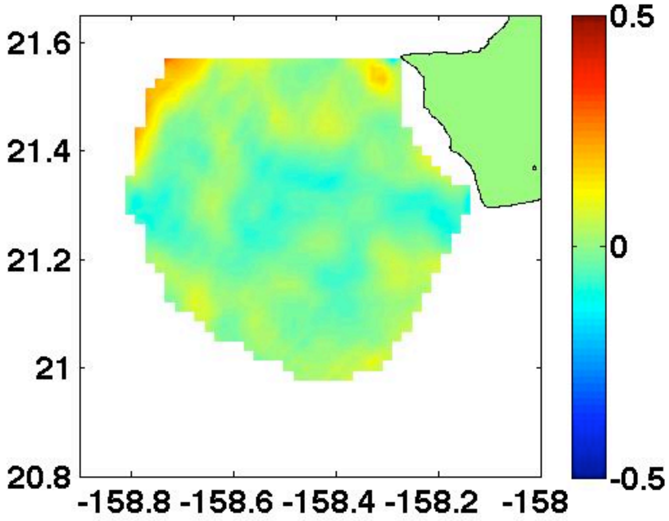

Fig. 32: Three month average divergence for September through November, 2002 using detided currents. Divergence (1/s) shown here normalized by Coriolis parameter.

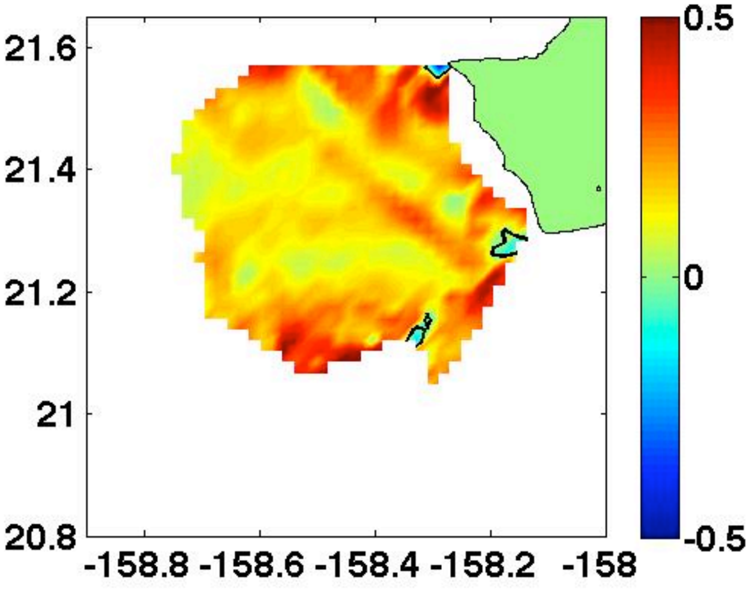

Fig. 33: Three month averaged Instantaneous RoS for February through April, 2002 using detided currents. Instantaneous RoS (1/s) shown here normalized by Coriolis parameter.

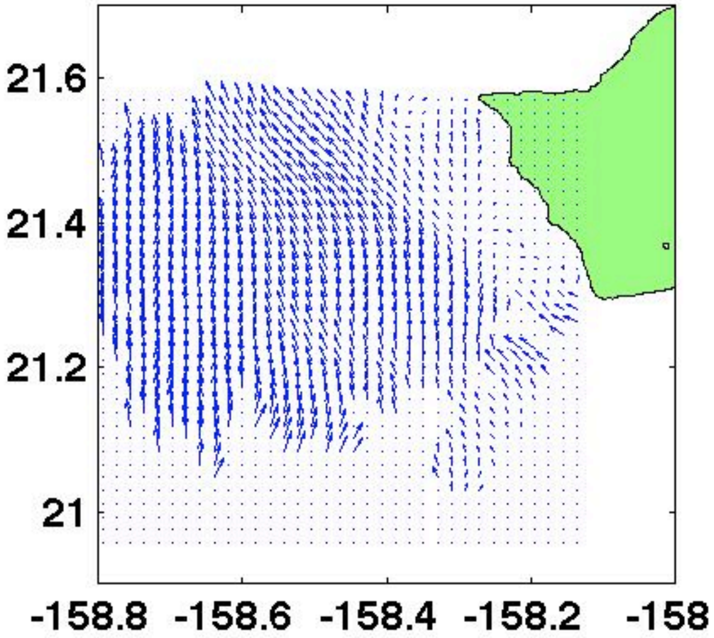

Fig. 34: Average surface current vectors from February through April, 2003.

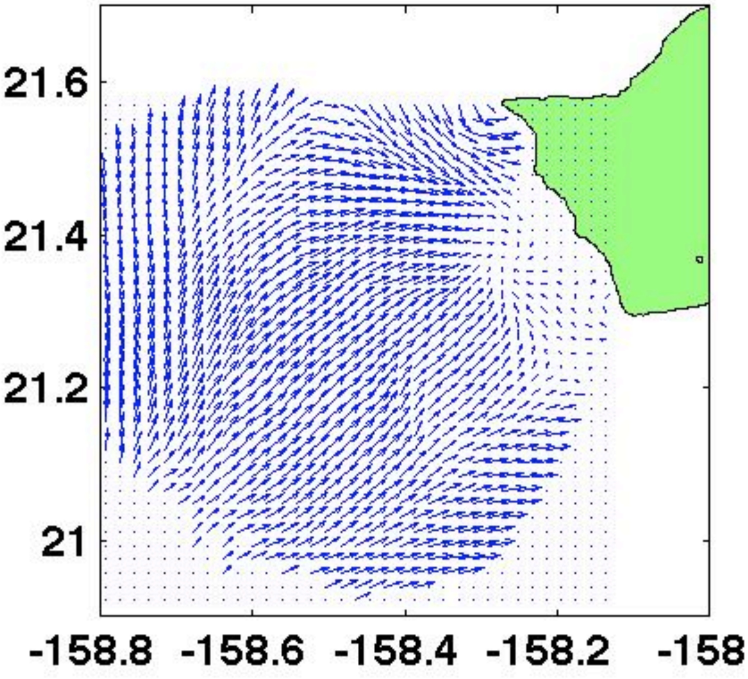

Fig. 35: Average surface current vectors from September through November, 2002.

Chapter 5

Particle Behavior during an Eddy Event

5.1 Introduction

Starting on October 24, 2002, an anticyclonic eddy began to develop in the lee of Oahu and in the middle of the HF radar coverage. The anticyclonic eddy persisted in the region until November 1, 2002 when its signal was no longer detectable in the HF radar data. Fig. 36 shows snapshots of the HF radar data during four stages in the eddy's lifespan, from development on October 24th to disappearance on November 1st. The anticyclonic eddy was also fairly stationary during its appearance in the HF Radar velocity field. The eddy had a strong core, with vorticity values (normalized by *f,* the Coriolis parameter) exceeding minus 1 (Fig. 37).

5.2 Dispersion Patterns

The arrival of an eddy event drastically changes particle dispersion patterns. The core of the eddy is dominated by vorticity, which traps particles inside the eddy core. This behavior is evident in the histogram, Fig. 27, depicting particle exit time from Chapter 4. When the eddy is present, particle retention time is higher and there is a larger number of particles remaining inside the HF radar coverage area during the entire integration period of 100 hours. Outside of the core, the flow field is dominated by regions of high strain (Isern-Fontanet et al., 2004). A measure used to identify eddy cores is the Okubo-Weiss parameter, W, which is more easily remembered as the magnitude of strain versus vorticity. W is

$$W = \sigma_1^2 + \sigma_2^2 - \zeta^2 \tag{5.1}$$

where σ_1 and σ_2 are the two components of strain and ζ is vorticity. When W is negative, vorticity dominates the flow field, when W is positive, strain dominates. An eddy is identified by negative values in the core, surrounded by high values. The anticyclone off Oahu was identifiable from the data based on its strong vorticity dominated core, and surrounding regions of high strain (Fig. 38). All values of W calculated in this study were normalized by the square of Coriolis parameter, *f*, to keep units in line with other analysis methods.

When particles trapped within the core of an eddy reach the outer core, they can be caught in these regions of high strain and escape. Particles originally outside the eddy can be drawn into the core as well. These dynamics could be seen in the anticyclonic eddy in the lee of Oahu. Particle trajectories simulated using the HF radar currents during the anticyclone, show the particles being drawn into the anticyclonic eddy (Fig. 39). Two trajectories, originating outside the eddy core, are tracked for 100 hours. Both trajectories skirt the core, but when they reach the high strain barrier, are drawn into the eddy and track away towards the anticyclone. It is these areas of high stretching where we expect high Lagrangian RoS values and high Instantaneous RoS values.

In the early stages of the anticyclone, regions of high stretching are visible outside the eddy core. The Instantaneous RoS field for October 24, 2002 at noon shows many interesting features (Fig. 40). Most notable is the region of high stretching originating just south of Kaena point, the NorthWest corner of Oahu. Particles to the south of this ridge are returned to the eddy core, where particles north of this ridge are expelled from the eddy. There is also a hint of a weaker ridge south of the anticyclone. The area inside these two ridges is an area of relatively low Instantaneous RoS values, indicating that particles are not separating quickly. Two days later, the ridge of high Instantaneous RoS off of Kaena Pt. is still evident, but has retracted back towards the island (Fig. 41). A second ridge has also begun to develop off of Barber's Pt. The ridge to the south of the eddy is more pronounced. Particles to the north of the ridge are returned to the North and towards the anticyclone. Particles to the south quickly exit the HF radar coverage area.

During the mature phase of the anticyclone, (Fig. 42), well developed regions of stretching, are dominating particle dispersion. Particles are trapped by these features, or expelled by these features. The most prominent features are on the outer edge of the anticyclone. As the anticyclone begins to decay and move out of the HF radar coverage area, the Instantaneous RoS ridges take on complicated forms (Fig. 43). Particles are no longer trapped by the anticyclone. A residual circulation exists, but the main coherent structures are to the West of this circulation.

As evident from the discussion above, the regions of high stretching and Instantaneous RoS are not simple. The regions of high stretching surround areas dominated by vorticity, but they are not consistent throughout the anticyclone's lifespan or always easily explained by the anticyclone itself. The anticyclone is a variable feature and is not comprised of pure vorticity. This variability creates complicated dynamics in the HF Radar field. The assumption that particles remain close together inside an eddy is not a safe assumption for a SAR application. If a SAR was to reach the outside of the core, they could easily be transported in a complete new direction.

Besides inherent variability in the eddy, other processes such as tidal impacts and interaction with other submesoscale features impact the dynamics in the HF radar field, causing regions of high separation coefficient that are not otherwise explainable.

5.3 Interaction with a localized front

The anticyclone observed by the HF radar was trapped alongside the coast of Oahu by two large cyclones, West and South of the anticyclone's center (Chavanne et al., 2008a). The interactions between these three eddy events caused warm water to be advected Northwards, creating a localized meridional front between -158.8 and -158.6 degrees longitude (Chavanne, et al., 2008a). The front was first visible using the Instantaneous RoS on October 27, 2002 (Fig. 44). Chavanne et al, 2008a identified the front as early as October 23, 2002 using sea surface temperature data (Fig. 45), but did not detect active frontogensis until October 26, 2002. The Instantaneous RoS, a measure of strain and divergence in the velocity field, would not pick up the front until it became active. Then the high strain associated with frontogensis would create ridges in the Instantaneous RoS, indicating areas where particles advected in the flow would be subjected to the affects of frontogensis.

Four particles released into the velocity field during the active frontogensis phase on October 28, 2002 all exhibit different behavior (Fig. 46). Two particles are released into the region dominated by the anticyclone. These particles follow the anticyclonic flow and travel parallel to regions of high Instantaneous RoS. Two particles were released into the region of active frontogensis, these particles experienced more chaotic behavior.

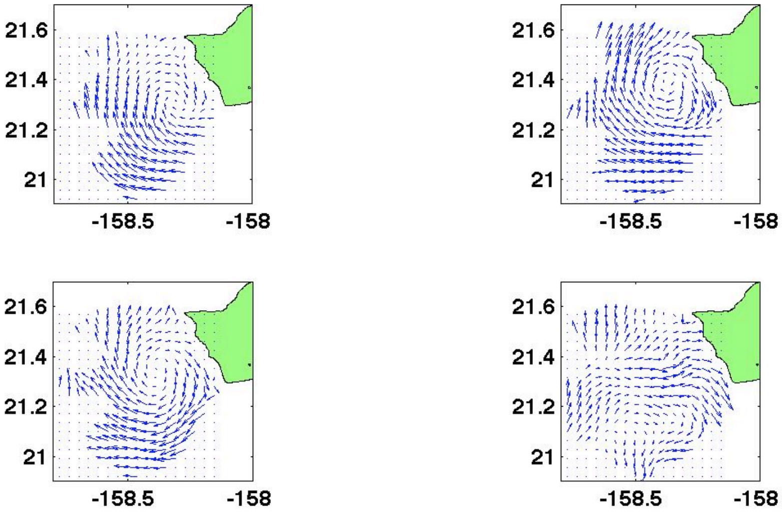

Fig. 36: Daily averaged currents for Top Left: October 24, 2002, Top Right: October 26, 2002, Bottom Left: October 28, 2002, Bottom Right: November 1, 2002.

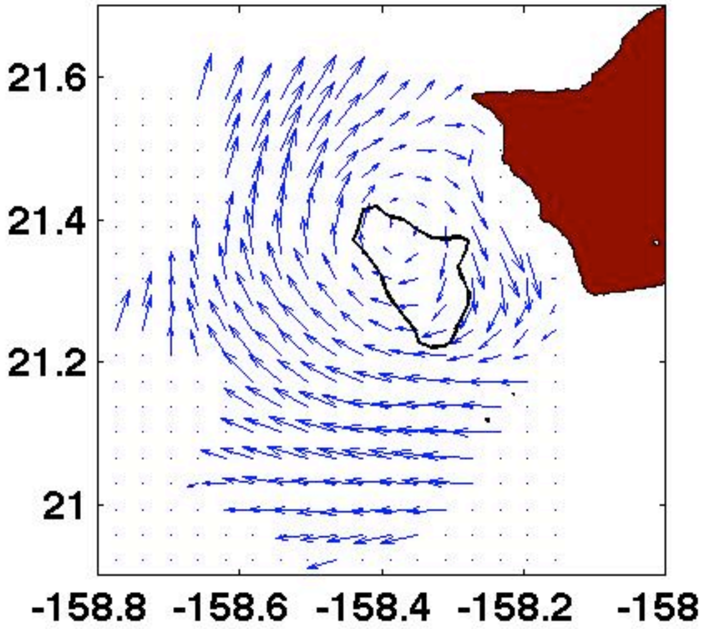

Fig. 37: Daily averaged currents for October 26, 2002. The thick black line represents the contour where the vorticity normalized by the Coriolis parameter is less than minus 1.

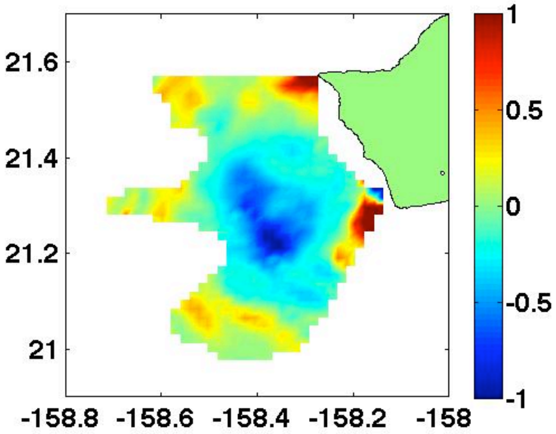

Fig. 38: The averaged magnitude of strain versus vorticity for October 28, 2002. Blue represents vorticity dominated regions, red represents strain dominated regions. Units ($1/s^2$) have been normalized by the square of the Coriolis parameter.

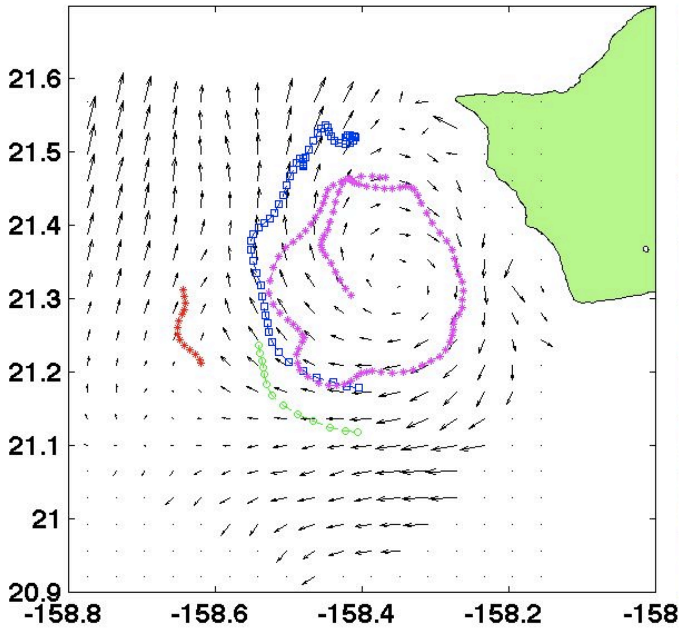

Fig 39: Particle trajectories during the anticyclonic eddy. Two trajectories remained inside the eddy until the end of the integration, however the two particles in the region of high strain quickly exited the HF Radar coverage.

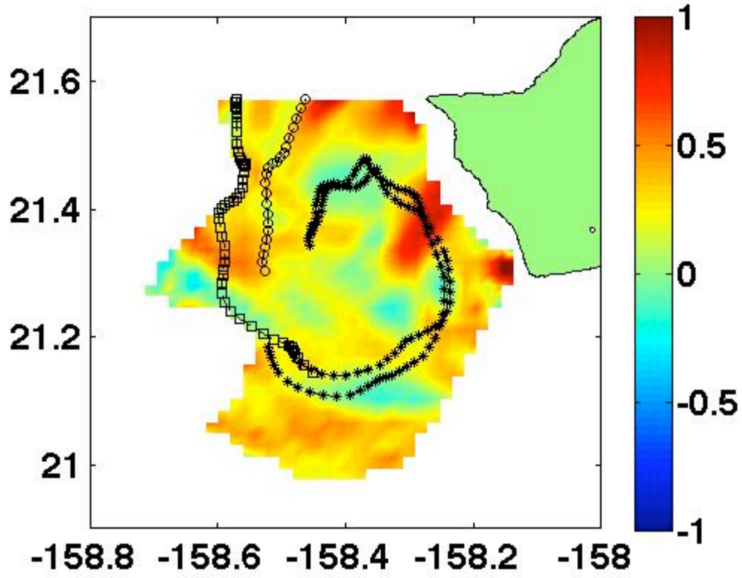

Fig. 40: Instantaneous RoS for October 24, 2002 at 1200. Black lines are particle trajectories released into the flow at that time. Instantaneous RoS (1/s) shown here normalized by Coriolis parameter.

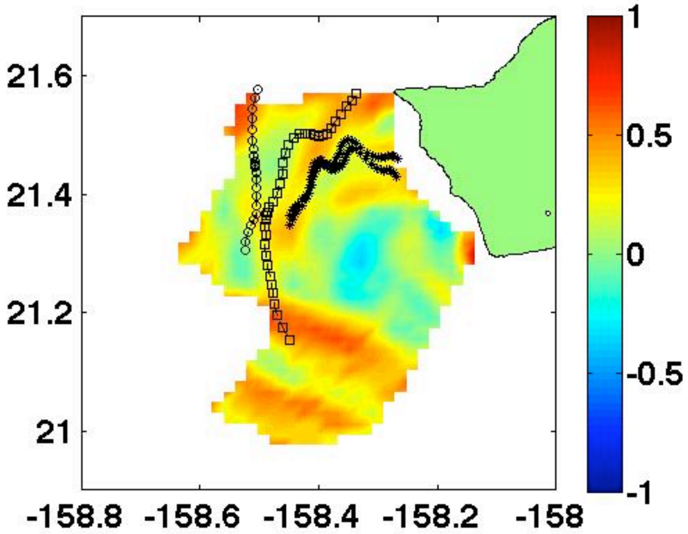

Fig.41: Instantaneous RoS for October 26, 2002 at 1200. Black lines are particle trajectories released into the flow at that time. Instantaneous RoS (1/s) shown here normalized by Coriolis parameter.

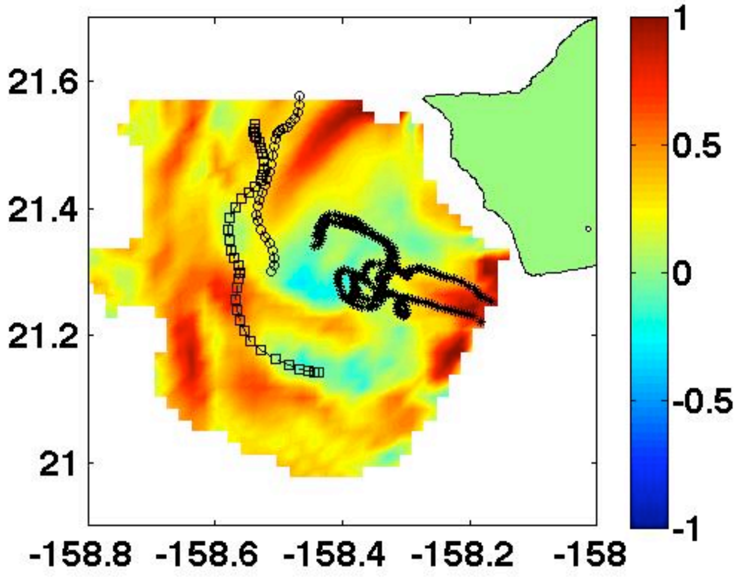

Fig 42: Instantaneous RoS for October 28, 2002 at 1900. Black lines are particles trajectories released into the flow at that time. Instantaneous RoS (1/s) shown here normalized by Coriolis parameter.

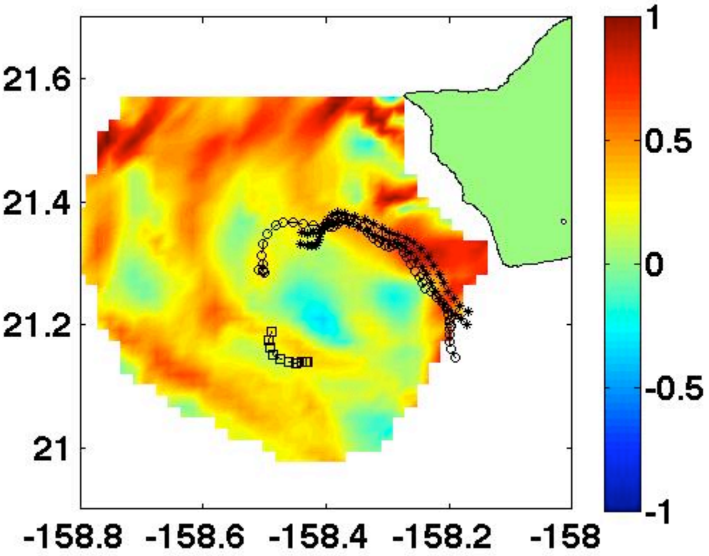

Fig. 43: Instantaneous RoS for November 1, 2002 at 2300. Black lines are particle trajectories initiated at the time of calculation. Instantaneous RoS (1/s) shown here normalized by Coriolis parameter.

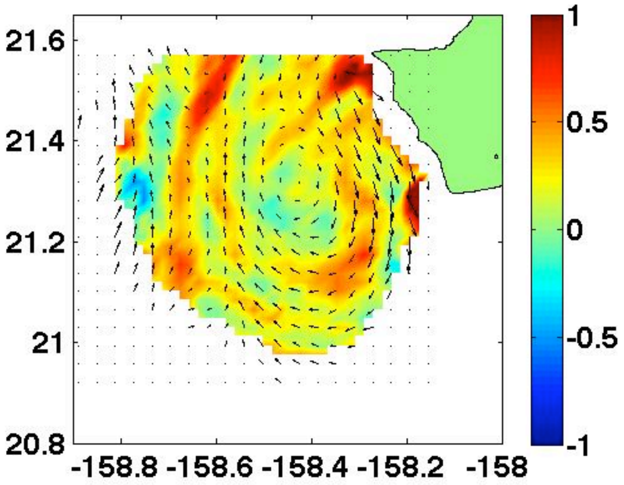

Fig. 44: Instantaneous RoS for October 28, 2002 at 0300. Instantaneous RoS (1/s) shown here normalized by Coriolis parameter.

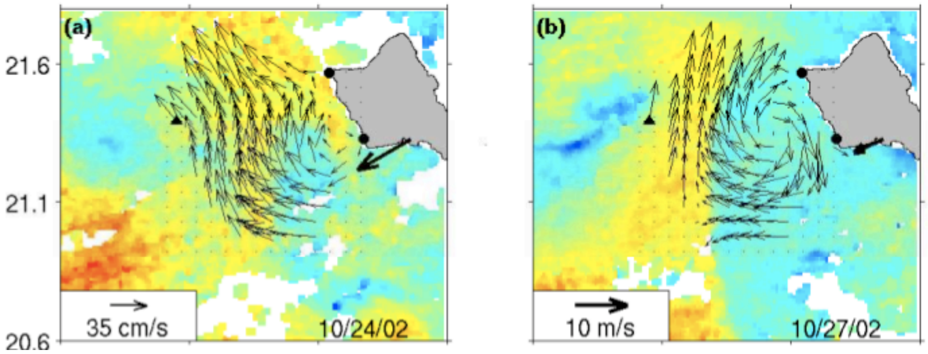

Fig. 45: SST front on October 24, 2002 and October 27, 2002. From (Chavanne et al., 2008a).

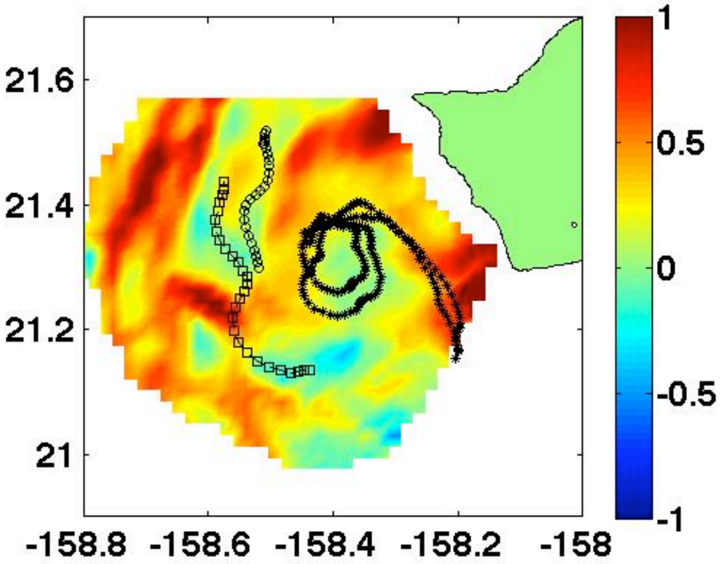

Fig 46: Instantaneous RoS for October 28, 2002. Black lines are particle trajectories initiated at time of calculation. Two particles started on the outer edge of the anticyclonic eddy and two particles started to the East of the front. Instantaneous RoS (1/s) shown here normalized by Coriolis parameter.

Chapter 6

Tidal Impacts

6.1 Introduction

The impact of tides on particle separation cannot be discounted. The oscillatory motion of tides aids in mixing through motions such as shear dispersion, chaotic stirring, and internal wave generation (Smith et al., 1997). Tidal currents can be derived from the HF radar total currents by extracting out the complex amplitudes of the dominant tidal constituents (Zaron et al., *submitted*). This chapter discusses the impacts of both surface tides and internal tides on particle separation behavior, and the ability of both the Lagrangian RoS and the Instantaneous RoS to identify tidal features from HF Radar data.

6.2 Surface Tidal Currents

Surface tidal currents are relatively weak around Oahu. The National Oceanographic and Atmospheric Administration (NOAA) lists the average tidal range as 1.2 feet with tidal currents ranging from weak and variable to 0.5 knots. Fig. 47 shows the tidal currents extracted from the HF radar data on October 18, 2002 for midnight, 0600, 1200, and 1800 hours. Particle trajectories were simulated from tidal currents to estimate the effect of drift due to tidal oscillations. After 100 hours, particles originally initiated on October 18, 2002 at 0600 hours looped around themselves and demonstrated very little drift from their original position (Fig. 48). This behavior was consistent throughout the study, indicating that residual tidal currents are not significant to particle separation rates in the coverage area. Given this result, the Instantaneous RoS and

Lagrangian RoS calculated from HF Radar data with tides included and from detided currents should be very similar. This is not usually the case.

The Lagrangian RoS was calculated using only tidal currents for 1h, 6h, and 12h time periods. The Instantaneous RoS was calculated every hour using only tidal currents extracted from HF Radar data. For October 18, 2002 at 0600, the Instantaneous RoS shows strong areas of strain and divergence off Ko'olina radar site (Fig. 49). The Instantaneous RoS calculated from detided currents for the same time period, shows much weaker values (Fig. 50). A simple addition of the Instantaneous RoS values using tidal currents only (Fig. 51) to the Instantaneous RoS using detided currents does not equal the values gained using total currents, indicating a non-linear relationship between the two. The Lagrangian RoS yield comparable relationships between total currents, detided currents, and tidal currents calculations during the study.

There are two processes which could be responsible for the impact of tides on particle separation. One is the stretching and stirring caused by the oscillatory motion of tides. Work done by Smith et al., 1997 found that the first few tidal cycles after a tracer patch was released caused stretching and splitting of the tracer patch. This stretching rapidly increased the dilution rate. A second, highly related process, is the impact of shear dispersion due to tidal oscillations. Taylor (1953) first described shear dispersion by discussing the dispersion of a tracer by laminar flow through a pipe. Taylor found that the sheared velocity in a piper enhanced the down-flow dispersion of the tracer. Later work by Young et al., 1982 and Young et al., 1991 looked for solutions to the advection-diffusion equation for more situations that those discussed by Taylor (1953) such as shear dispersion in a flow with sinusoidal vertical structure, and in well mixed estuaries. In this study, the oscillatory motion of the tides causes shear which enhances particle diffusion rates.

Shear dispersion can be a prominent mechanism for particle separation when combined with large scale features such as the front observed from October 26-29, 2002. Fig. 52 shows the front picked up by the Instantaneous RoS using total currents on October 28, 2002 at 0600. Fig. 53 shows the same results using detided currents. The strength of the Instantaneous RoS from detided currents at the location of the front is weaker than the results from the total currents. The ebb and flow of the tide could be causing enhancement of particle separation rates due to shear dispersion.

6.3 Internal Tides

Another tidal feature which can impact dispersion is internal tides. Kaena Ridge, located to the northwest of Oahu produces energetic semidiurnal internal tides (Aucan et al., 2005). The bathymetry of Kauai channel, located between the island of Kauai and Oahu is shown in Fig. 54. The internal tides generated at Kaena ridge radiates two energy beams towards the South: one radiates downwards towards the bottom, the second towards the surface (Nash et al, 2005). There have been many recent studies on the energetics and mixing of internal tides generated at Kaena Ridge, such as Nash et al., 2006; Aucan et al., 2005; and Klymak et al., 2007. Because HF Radars only measure the top 1.5 meters of the ocean's surface, a direct study of mixing due to internal waves is not possible here, however the beam propagating towards the surface can be picked up by the HF radar data and the Instantaneous RoS. Chavanne, 2007 picked up the internal tide surface signature using semi-diurnal kinetic energy calculated from the HF Radar currents (Fig. 55). The internal tide signal likely identified using the Instantaneous RoS for the corresponding day is visible on November 5, 2002 (Fig. 56) by the large zonal ridge depicted in the Instantaneous RoS at around 21.3 degrees latitude. The total current velocities measured from the HF radar are plotted in conjunction with the Instantaneous RoS. From just observing patterns in current direction alone, it is hard to pick out any internal tide signal. However, the strain rate and divergence rate measured from the HF radar currents produces a very strong internal tide signal. The internal tide signal is visible multiple times throughout the study, in approximately the same location each time. The internal tide signal was visible again on November 3, 2002 and November 7, 2002.

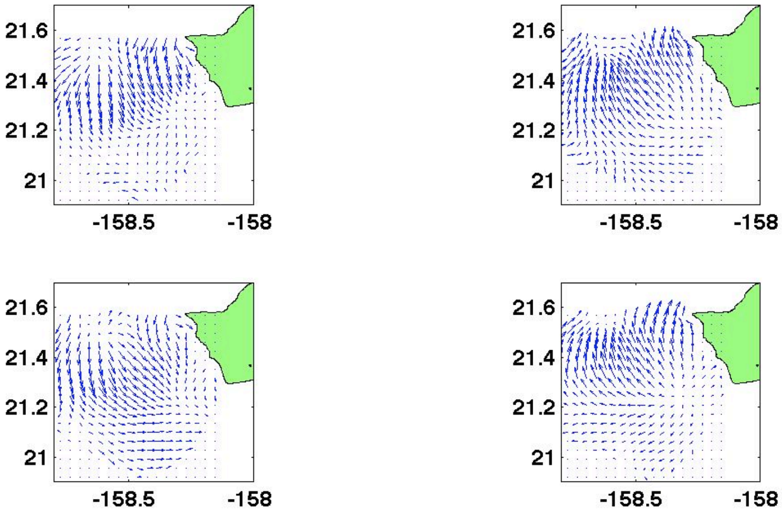

Fig. 47: Tidal currents generated from the HF Radar data for October 18, 2002. Top Left: 0000 hours, Top Right: 0600 hours, Bottom Left: 12000 hours, Bottom Right: 1800 hours. Velocity vectors have been scaled 150%.

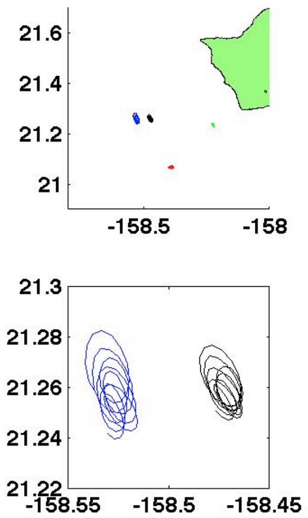

Fig. 48: Four particle trajectories initiated on October 18, 2002 at 0600 hours. The bottom panel is a smaller scale area of two of the particle trajectories shown in the top panel.

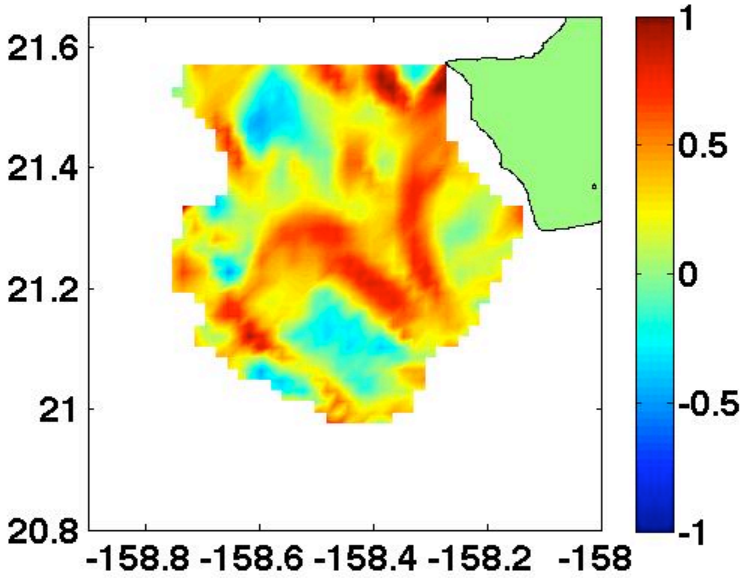

Fig. 49: Instantaneous RoS for October 18, 2002 at 0600 using total currents (tides included) from HF Radar data. Instantaneous RoS (1/s) shown here normalized by Coriolis parameter.

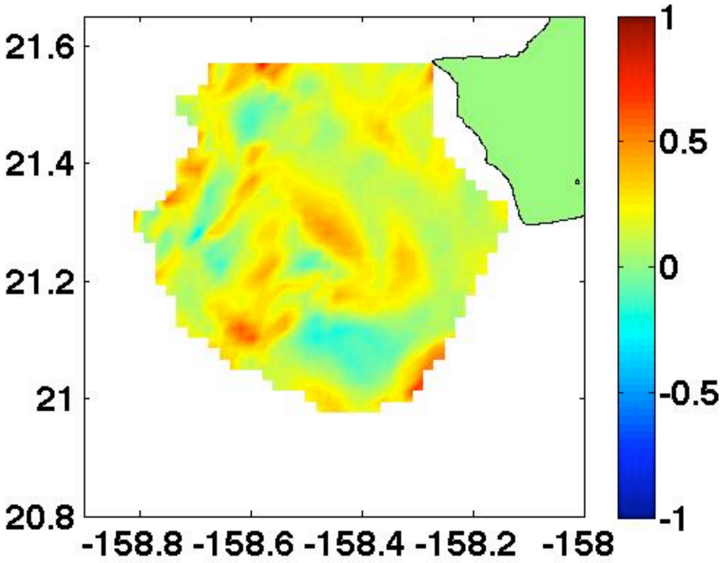

Fig. 50: Instantaneous RoS for October 18, 2002 at 0600 using detided currents. Instantaneous RoS (1/s) shown here normalized by Coriolis parameter.

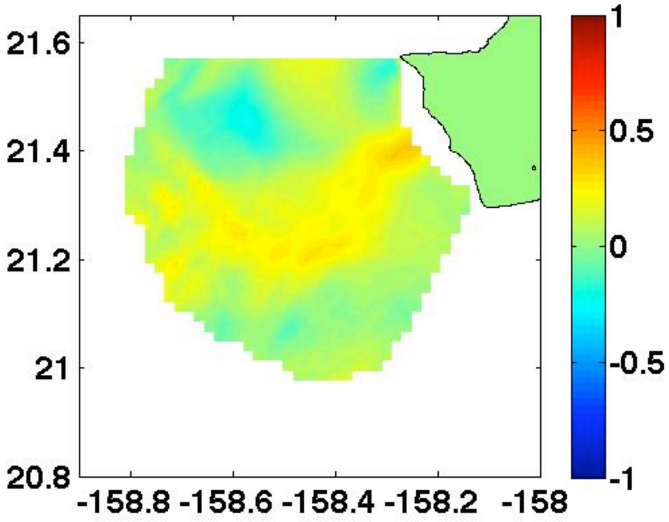

Fig. 51: Instantaneous RoS using only tidal currents for October 18, 2002 at 0600 hours. Instantaneous RoS (1/s) shown here normalized by Coriolis parameter.

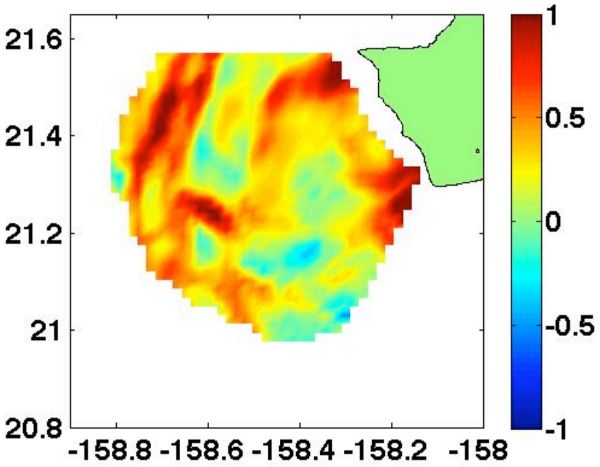

Fig. 52: Instantaneous RoS using total currents for October 28, 2002 at 0600 during active frontogensis. Instantaneous RoS (1/s) shown here normalized by Coriolis parameter.

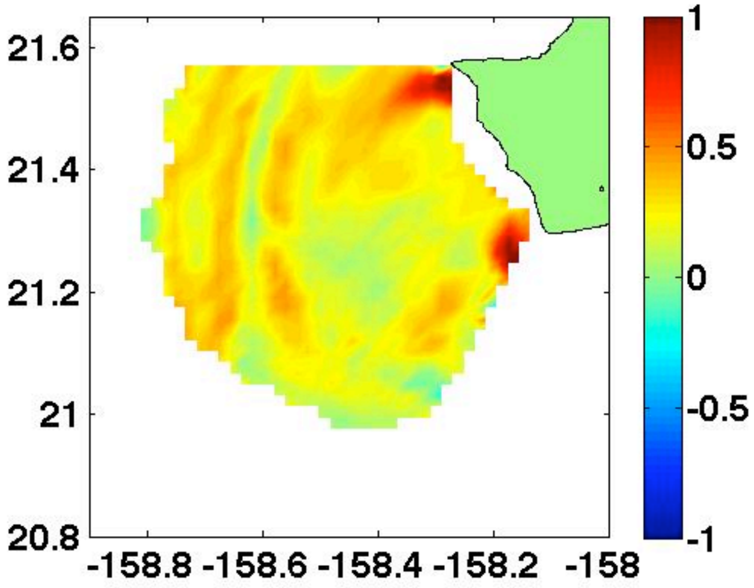

Fig. 53: Instantaneous RoS using detided currents for October 28, 2002 at 0600 hours during active frontogensis. Instantaneous RoS (1/s) shown here normalized by Coriolis parameter.

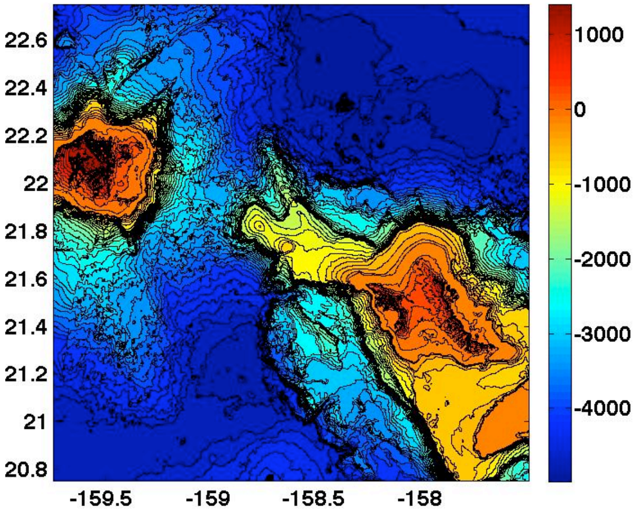

Fig. 54: Bathymetry of Kauai channel, between the islands of Oahu and Kauai. Depth in meters.

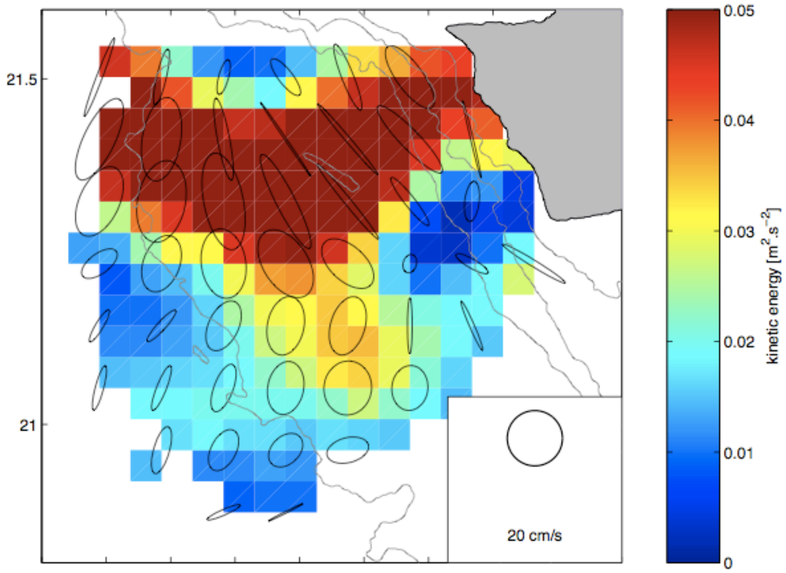

Fig. 55: Semi-diurnal kinetic energy for November 5, 2002. From Chavanne, 2007.

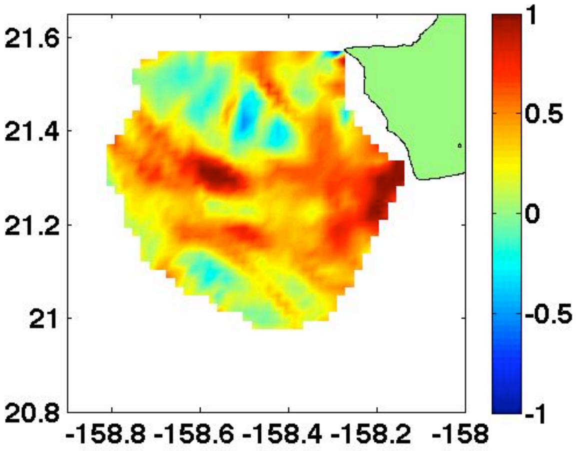

Fig. 56: Instantaneous RoS for November 5, 2002 using total currents. Instantaneous RoS (1/s) shown here normalized by Coriolis parameter

Chapter 7

Conclusions

The flow to the west of Oahu is quite dynamic and provides a challenging setting for operations such as search and rescue or pollution mitigation. Particle dispersion and separation rates are dominated by seasonal trends, tidal impacts and large scale features. Seasonally, particles retention is higher in the fall, when current velocities are slightly lower. In the spring, particle retention is lower: steady direction and faster current velocities usher particles out of the HF radar coverage sooner. Surface tidal impacts are small, but when combined with large features, such as a front, can impact dispersion properties through shear dispersion. Finally, island dynamics produce eddy events which can either trap particles in its core, or disperse particles in the regions of high strain that surround the eddy, however these regions are highly variable over the lifespan of the eddy. The topography beneath the water can also add complexity by generating energetic internal tides which surface in the lee of Oahu.

Previous studies used the Lagrangian RoS to quantify mixing and stretching in a flow field (d'Ovidio et al., 2004; Haller, 2002; Peng and Dabiri, 2009). Here a new method was tested, the Instantaneous RoS. The Instantaneous RoS is derived from the Lagrangian RoS and high values represent areas of high strain and/or divergence. The Instantaneous RoS, was sensitive enough to pick up local fronts in both total currents and in tidal currents, as well as internal tide signatures. Discounting the lag between the Lagrangian RoS and the Instantaneous RoS that is caused by different calculation methods, there was good agreement between the two computations during the course of the study The agreement between the Instantaneous RoS and the 1 hour fixed time Lagrangian RoS is encouraging. Actual deployment of SLDMB's in regions of high Instantaneous RoS to quantify how far drifters actual separate in these zones would be a good verification of this study. This would also provide a more accurate correlation between Instantaneous and Lagrangian RoS values, possible allowing for the computation of a Rate of Separation coefficient. The Instantaneous RoS has a lot of potential to assist in SAR cases, but verification of this work with surface drifting buoys is needed before any quantification of applicability could be stated with conviction.

References

Artale, V., G. Boffeta, A. Celani, M. Cencini, A. Vulpiani, 1997. Dispersion of passive tracers in closed basins: Beyond the diffusion coefficient, *Phys. Fluids*, **9**:3162-3171

Bracco, A., J. Hardenberg, A. Provenzale, J.B.Weiss, J.C.McWilliams, 2004. Dispersion and Mixing in Quasigeostrophic Turbulence, *Phys Rev Lett*, **92**:084501

Canuto, V.M., A. Howard, Y. Cheng, M.S. Dubovikov, 2001. Ocean Turbulence. Part 1: One-Point Closure Model--Momentum and Heat Vertical Diffusivities, *J. Phys. Oceanog.,* **31**: 1413-1426

Chavanne, C., P. Flament, R. Lumpkin, B. Dousset, A. Bentamy, 2002. Scatterometer observations of wind variations induced by oceanic islands: Implications for wind-drive ocean circulation, *Can. J. Remote Sensing*, **28**: 466-474

Coulliette, C., F. Leiken, J. Paduan, G. Haller, J. Marsden, 2007. Optimal Pollution Mitigation in Monterey Bay Based on Coastal Radar Data and Nonlinear Dynamics, *Environ. Sci. Technol.,* **41**: 6562-6572

Csanady, G. T., 1973. *Turbulent Diffusion in the Environment*. Reidel, Dordrecht.

d'Ovidio, F., V. Fernandez, E. Hernandez-Garcia, C. Lopez, 2004. Mixing structures in the Mediterranean Sea from finite-size Lyapunov exponents, *Geophys. Research Letters,* **31**, L17203.

Flament, P., L. Armi, 2000. The shear, convergence, and the thermohaline strucure of a front, *J. Phys. Oceanog.,* **30**:51-66

Flament, P., S. C. Kennan, R. A. Knox, P. P. Niiler, R. L. Bernstein, 1996. The three-dimensional structure of an upper ocean vortex in the tropical Pacific Ocean, *Nature*, **383**:610-613

Haller, G., 2002. Lagrangian coherent structures from approximate velocity data, *Phys. Fluids*, **14**:1851-1861

Haller, G., G., Yuan, 2000. Lagrangian coherent structures and mixing in two-dimensional turbuluence, *Physica D*, **147**:352-370

Kennan, S. C., P. J. Flament, 2000. Observations of a tropical instability vortex, *J. Phys. Oceanog.,***30**:2277-2301

LaCasce, J.H., 2008. Statistics from Lagrangian observations, *Progress in Oceanography,* **77**:1-29

LaCasce, J.H., A. Bower, 2000. Relative dispersion in the subsurface North Atlantic, *J. Mar. Research*, **58**:863-894

LaCasce, J.H., C. Ohlmann, 2003. Relative dispersion at the surface of the Gulf of Mexico, *J. Mar. Research*, **61**:285-312

Lekein, Y., F. d'Ovidio, M. Levy, E. Heifetz, 2007. Stirring of the northeast Atlantic spring bloom: A Lagrangian analysis based on multisatellite data, *J. Geophys. Research,* **112**, C08005

Lekein, F., C. Coulliette, A. J. Mariano, E. H. Ryan, L. K. Shay, G. Haller, J. Marsden, 2005. Pollution release tied to invariant manifolds: A case study for the coast of Florida, *Physica D*, **210**:1-20

Lumpkin, R., A. Treguier, K. Speer, 2002. Lagrangian Eddy Scales in the Northern Atlantic Ocean, *J. Phys. Oceanog.,* **32**:2425-2440

Marshall, J., E. Shuckburgh, H. Jones, C. Hall, 2006. Estimates and Implications of Surface Eddy Diffusivity in the Souther Ocean Derived from Tracer Transport, *J. Phys. Oceanog.,* **36**:1807-1821

McClean, J., P. Poulain, J. Pelton, M. Maltrud, 2002. Eulerian and Lagrangian Statistics from Surface Drifters and a High-Resolution POP Simulation in the North Atlantic, *J. Phys. Oceanog.,* **32**:2472-2491

Middleton, J. F., 1985. Drifter Spectra and diffusivities, *J. Mar. Research,* **43**:37-55

Nakamura, N., 1996. Two-Dimensional Mixing, Edge Formation, and Permeability Diagnosed in an Area Coordinate, *J. Atmos. Sci.,* **53**:1524-1537

Okubo, A., 1971. Oceanic diffusion diagrams, *Deep Sea Research*, **18:** 789-802.

Peng, J., J. O. Dabiri, 2009. Transport of inertial particles by Lagrangian coherent structures: application to predator-prey interaction in jellyfish feeding, *J. Fluid Mech.,* **623**:75-84

Press, W. H., S. A. Teukolsky, W. T. Vetterling, B. P. Flannery, 2007. *Numerical Recipes: The Art of Scientific Computing*, Cambridge University Press.

Shadden, S. C., F. Lekein, J. E. Marsden, 2005. Definition and properties of Lagrangian coherent structures from finite-time Lyapunov exponents in two-dimensional aperiodic flow, *Physica D*, **212**:271-304

Shadden, S. C., F. Lekein, J. D. Paduan, F. P. Chavez, J. E. Marsden, 2007. The correlation between surface drifters and coherent structures based on high-frequency radar data in Monterey Bay, *Deep Sea Res.,* submitted

Smith, R., C. F. Scott, 1997. Mixing in the Tidal Environment, *J. Hydraulic Engineering*, **123**:332:340

Ullman, D. S., J. O'Donnell, J. Kohut, T. Fake, A. Allen, 2006. Trajectory prediction using HF radar surface currents: Monte Carlo simulations of prediction uncertainties, *J. Geophys. Research*, **111**, C12005

Young, W. R., S. Jones, 1991. Shear Dispersion, *Phys. Fluids,* **3:**1087-1101

Young, W. R., P. B. Rhines, C. J. R., Garrett, 1982. Shear-Flow Dispersion, Internal Waves and Horizontal Mixing in the Ocean, *J. Phys. Oceanog.,* **12**:515-527